Entrainment in the Denmark Strait Overflow Plume by meso-scale Eddies

Gunnar Voet

August 2006

Diplomarbeit im Fach Physik
Universität Hamburg
Department Physik · Department Geowissenschaften
Angefertigt am Institut für Meereskunde

Betreuer: Prof. Dr. Detlef Quadfasel

Abstract

Denmark Strait Overflow Water is a major constituent of the North Atlantic Deep Water. When sinking into the Irminger Sea its volume transport approximately doubles by entrainment of ambient waters within the first 500 km downstream of the Denmark Strait sill. This overall amount of entrained water was estimated in previous studies, but the relative contributions of horizontal and vertical turbulent processes to the entrainment were not quantified yet.

Meso-scale eddies that reach from the overflow plume at the bottom up to the sea surface and travel with the overflow plume along the Greenland shelf slope are a persistent feature in the Denmark Strait Overflow. They can be identified in infrared satellite imagery at the surface as well as in current measurements close to the bottom.

The contribution of these meso-scale eddies to the entrainment into the overflow plume at three moorings arrays 200, 360 and 520 km downstream of the Denmark Strait sill is analysed in this work. An averaged heat transport equation is derived that explains the downstream plume warming through horizontal and vertical turbulent heat fluxes. Mean plume temperatures calculated from mooring timeseries and hydrographic sections provide information on the downstream plume warming, while horizontal eddy heat transports can be calculated from mooring array data.

It was found that the meso-scale eddies explain most of the increase in mean plume temperature in the region beyond 200 km downstream from the sill. The eddy induced warming rates of the plume core are $\sim$120 $^{\mathrm{mK}}/_{\mathrm{100km}}$ at the array closest to the sill, $\sim$160 $^{\mathrm{mK}}/_{\mathrm{100km}}$ in the centre mooring array and $\sim$50 $^{\mathrm{mK}}/_{\mathrm{100km}}$ at the mooring array 520 km downstream of the sill. The plume warming rate in the first 200 km downstream of the sill is $\sim$440 $^{\mathrm{mK}}/_{\mathrm{100km}}$ compared to 44–175 $^{\mathrm{mK}}/_{\mathrm{100km}}$ further downstream.

Eddy induced heat fluxes can not explain the high initial warming. It is concluded that vertical turbulent processes dominate the entrainment into the overflow plume during its first descent into the deep North Atlantic.

Zusammenfassung

Die Wassermassen des Dänemarkstraßen-Overflows sind ein Hauptbestandteil des Nordatlantischen Tiefenwassers. Beim Absinken in die Irminger See wird der Volumentransport des Overflows durch Einmischung ambienten Wassers (Entrainment) auf den ersten 500 km stromabwärts von der Schwelle der Dänemarkstraße ungefähr verdoppelt. Die Menge des Entrainments wurde in früheren Studien abgeschätzt. Der relative Anteil von horizontalen und vertikalen turbulenten Prozessen am Entrainment konnte bisher jedoch nicht quantifiziert werden.

Meso-skalige Wirbel (Eddies), die von der Overflow-Plume in der Tiefe bis an die Meeresoberfläche reichen und mit der Plume entlang der Grönländischen Kontinentalschelfkante wandern, sind eine beständige Eigenschaft des Overflows. Die Wirbel können sowohl in satellitengestützten Infrarotaufnahmen der Meeresoberfläche als auch in Strömungsmessungen am Boden nachgewiesen werden.

In dieser Arbeit wird der Beitrag der meso-skaligen Wirbel zum Entrainment in die Overflow-Plume in drei Verankerungsbereichen 200, 360 und 520 km stromabwärts der Dänemarkstraße untersucht. Eine gemittelte Wärmetransportgleichung wird hergeleitet, die stromabwärtige Erwärmung der Plume mit horizontalen und vertikalen turbulenten Wärmeflüssen erklärt. Die Berechnung mittlerer Plumetemperaturen aus Temperaturzeitserien und hydrographischen Schnitten gibt Auskunft über die stromabwärtige Erwärmung der Plume, während der durch Wirbel verursachte horizontale Wärmetransport aus Strömungs- und Temperaturzeitserien berechnet werden kann.

Diese Arbeit zeigt, dass die meso-skaligen Wirbel den größten Teil der Erwärmung der Plume im Bereich südlich von 200 km Entfernung zur Dänemarkstraße erklären können. Die durch Wirbel verursachten Aufwärmraten des Plumekerns sind $\sim$120 $^{\mathrm{mK}}/_{\mathrm{100km}}$ im Verankerungsbereich in 200 km Entfernung zur Dänemarkstraße, $\sim$160 $^{\mathrm{mK}}/_{\mathrm{100km}}$ im mittleren Verankerungsbereich und $\sim$50 $^{\mathrm{mK}}/_{\mathrm{100km}}$ im Verankerungsbereich 520 km stromabwärts von der Schwelle. Die Aufwärmrate der Plume ist $\sim$440 $^{\mathrm{mK}}/_{\mathrm{100km}}$ auf den ersten 200 km südlich der Schwelle in Vergleich zu Aufwärmraten zwischen 75 und 44 $^{\mathrm{mK}}/_{\mathrm{100km}}$ weiter stromabwärts.

Durch Wirbel angetriebene Wärmeflüsse können die anfängliche Aufwärmrate nicht erklären. Es wird gefolgert, dass vertikale Turbulenzprozesse das Entrainment in die Overflow-Plume beim ersten Absinken in die Irminger See dominieren.

Contents

List of Figures

1 Introduction

The ocean is a major heat source for the North Atlantic climate system. When the water looses its heat to the cold atmosphere it becomes denser and sinks. The density increase creates a deep large scale meridional pressure gradient that drives a southward flow. This flow of the dense watermasses at depth is compensated by a northward flow of warm water near the surface.

The southward flow in the deep and the northward flow at the surface in the Atlantic form a meridional circulation cell, the Atlantic Meridional Overturning Circulation. This circulation cell leads to a redistribution of heat from low to high latitudes. Recent studies suggest that the overturning circulation may weaken in the course of climate change (BRYDEN ET AL., 2005). This could have drastic ecological and socio-economical consequences in northern Europe.

The cell strength of the Atlantic Meridional Overturning Circulation, i. e. its volume transport, is around 18 Sv[1]. The two major areas where the surface waters are cooled and transformed into the deep dense watermasses are the Labrador Sea and the Nordic Seas[2]. The Labrador Sea contributes ~4–6 Sv, the Nordic Seas account for about 6 Sv. Another 6 Sv are still missing for the balance between deep and surface flow. Their origin becomes apparent when the pathway of the deep dense flow from the Nordic Seas into the North Atlantic is analysed more closely.

The outflow of dense waters from the Nordic Seas is blocked by the Greenland-Scotland Ridge. The Greenland-Scotland Ridge is a shallow ridge separating the Nordic Seas from the North Atlantic. Iceland and the Faroe Islands are the parts of the ridge that rise above the sea level. Only two deep passages in the ridge, the Faroe-Bank Channel and Denmark Strait, east and west of Iceland, allow a substantial outflow of dense water. They have sill depths of 840 m and 600 m, respectively. Approximately half of the outflow from the Nordic Seas crosses the Greenland-Scotland ridge east of Iceland. The other half passes through Denmark Strait west of Iceland. This thesis is concerned with the overflow through Denmark Strait.

After crossing the sill of Denmark Strait, the dense water flows along the Greenland continental slope. It descends as a narrow plume into the deep North Atlantic and feeds the North Atlantic Deep Water. The volume of the dense overflow current increases by mixing of ambient water into the plume and its density decreases (Fig. 1.2). This process is called entrainment. The entrainment into the Denmark

---

[1] 1 Sverdrup = 10^6 $\mathrm{m^3/s}$.

[2] The Nordic Seas subsume the Iceland, Greenland and Norwegian Seas.

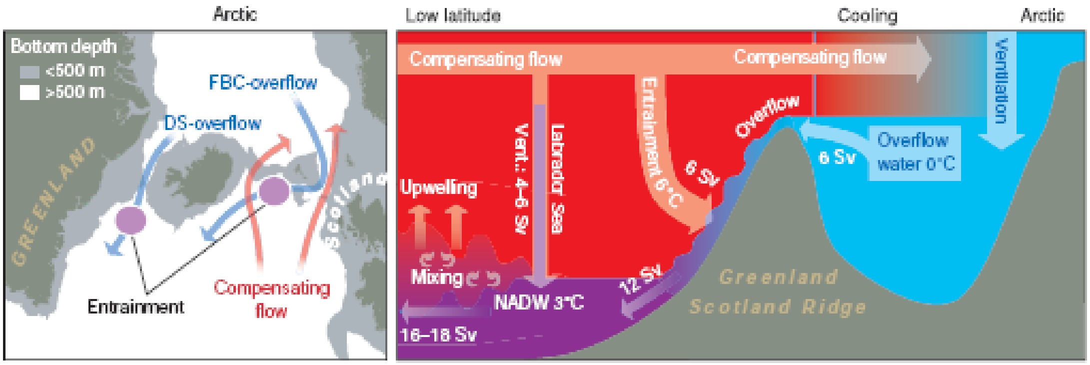

Figure 1.1: *Exchange of water across the Greenland-Scotland Ridge as a component of the Atlantic Meridional Overturning Circulation. The map on the left shows the shallow Greenland-Scotland Ridge with the Denmark Strait (DS) and the Faroe Bank Channel (FBC) west and east of Iceland. The dense overflows are shown as blue arrows. The compensating inflow is shown with red arrows. Entrainment regions are marked with purple circles. On the schematic section on the right, the formation of the North Atlantic Deep Water (NADW) is shown. Temperatures are given in °C and volume transports in Sv are approximate values. The two ventilation regions are the Arctic and the Labrador Sea. The entrainment into the overflow plumes contributes to the formation of NADW. The mixing at low latitudes is shown as it is needed for driving the circulation. From* HANSEN ET AL. *(2004).*

Strait overflow plume leads to a doubling of the plume volume transport between the sill and 520 km downstream. Entrainment thus is the missing third source for the deep branch of the Atlantic Meridional Overturning Circulation. Hence, the southward flowing North Atlantic Deep Water consists of about $^1/_3$ Labrador Sea Water, $^1/_3$ overflow water from the Nordic Seas and $^1/_3$ entrained ambient water.

The mixing of watermasses with different temperature and salinity corresponds to an exchange of heat and salt. Physically, this exchange is a diffusive flux across a gradient, i. e. a process on a molecular level. Molecular diffusion is a slow process which can be greatly enhanced, when the interfacial area between the water masses is increased. A larger interface may be generated by turbulent processes like breaking internal waves, tides or vortices.

The overall amount of entrainment into the Denmark Strait Overflow plume was estimated in previous studies, but the relative contributions of horizontal and vertical turbulent processes to the entrainment were not quantified yet.

A fascinating process that accompanies the Denmark Strait Overflow is the formation of meso-scale eddies[3]. They reach from the overflow plume at the bottom up to the sea surface. The eddies can be identified in infrared satellite imagery at the surface as well as in current measurements close to the bottom. They travel with the overflow plume along the continental slope. Eddies are a persistent feature of the

---

[3] A small vortex under the influence of the rotation of the earth is called eddy in fluid dynamics.

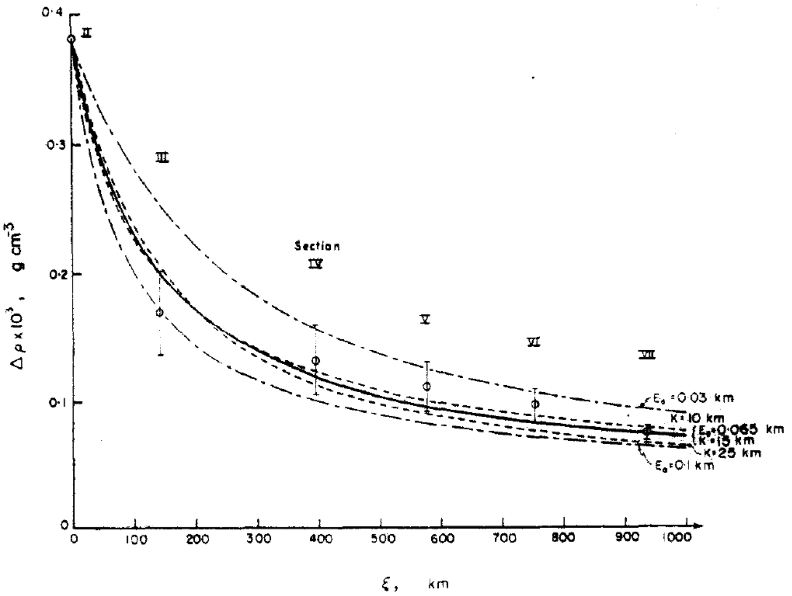

Figure 1.2: *Change of average density contrast* $\Delta\,\rho$ *in the Denmark Strait Overflow. The average density contrast (difference between overflow plume density and local ambient density) is shown in measured data (open circles with errorbars) and in streamtube model results for different empirical constants for entrainment and bottom stress (lines).* ξ *denotes the downstream distance from the sill. From* Smith *(1975).*

Denmark Strait Overflow. The eddies can be reproduced in numerical simulations of the overflow as well as in laboratory experiments with rotating tanks.

The aim of this work is to estimate how much the observed eddies contribute to the entrainment into the Denmark Strait Overflow plume.

Data from mooring arrays on the Greenland continental slope downstream of Denmark Strait sill provide information on temperature and current direction and velocity of the plume. The horizontal eddy heat transports into the plume are calculated with these data. A comparison with the warming of the overflow plume on its way downstream then gives an estimate for the importance of eddies in the entrainment process.

General circulation models used in climate prediction are too coarse to resolve eddies in the Denmark Strait Overflow. The knowledge about a possible contribution of eddies to the entrainment in the overflow is valuable for an improvement of the parameterisation of entrainment in the numerical models.

The thesis is structured as follows:

- **Chapter two** starts with a short review of the Denmark Strait Overflow. Physical mechanisms and previous studies of eddy generation processes are presented. The heat transport equation that forms a basis for this study is derived.

- In **chapter three** current meter instruments are presented and data analysis methods are explained.
- **Chapter four** describes the characteristic structure of the overflow plume at the Angmagssalik mooring array 520 km downstream of the Denmark Strait sill. The eddy heat transport into the cold plume is calculated. A warming of the plume core that is driven by the eddies is found.
- The same is done in **chapter five** for the two mooring arrays Dohrn and TTO closer to the Denmark Strait sill. The eddy induced warming of the plume core is found to be stronger than in the Angmagssalik array.
- In **chapter six** the downstream warming of the overflow plume is estimated from temperature measurements in mooring arrays and hydrographic surveys.
- In **Chapter seven** the overall plume warming is compared with eddy driven warming rates. It is found that the eddies can explain the plume warming in the three mooring arrays.
- **Chapter eight** links the results found in this the work to general climate research and emphasises the need for a better understanding of the entrainment processes. Proposals for further studies of the entrainment into the Denmark Strait Overflow plume are made.

2 The Denmark Strait Overflow and associated downstream processes

This chapter gives a brief review of the general circulation across the Greenland-Scotland Ridge, the topography of the Denmark Strait region, the properties of the Denmark Strait Overflow Water and its origin. Past observations and explanation approaches for vortex formation and high variability on transient time scales downstream of the Denmark Strait sill are summarised. The basic physical processes of mixing and entrainment are explained. An averaged heat equation is derived that describes turbulent mixing processes. Finally, the results of past studies on entrainment are presented.

2.1 A short review of the Denmark Strait Overflow

The Denmark Strait Overflow (DSO) is the western part of the deep overflows across the Greenland-Scotland Ridge (GSR). The bathymetry and general circulation scheme of this area are shown in Fig. 2.1.

The Denmark Strait Overflow Water (DSOW) was defined by SWIFT ET AL. (1980) in the density range of $27.95 \leq \sigma_\theta \leq 28.0$. DICKSON AND BROWN (1994) take $\sigma_\theta \geq 27.80$ while TANHUA ET AL. (2005) use $\sigma_\theta = 27.88$, based on recent results from an experiment with SF_6 tracers[1]. Isotherms can also be used to define the boundary of the overflow plume.

The DSO is fed by intermediate waters from the Arctic Ocean and the Nordic Seas. There is no consensus on the path of the source waters to the Denmark Strait[2] (DS). Recent numerical simulations show that the DSO is supplied by two different source pathways (KÖHL ET AL., 2006).

---

[1] SF_6 is a chemical tracer that allows to identify the origin of a watermass.

[2] While prior studies suggested the East Greenland Current (EGC) to feed the overflow (e.g. RUDELS ET AL. (2002)), a more recent study by JÓNSSON AND VALDIMARSSON (2004) reports on a current that runs along the Icelandic slope and transports water from the Iceland Sea north of Iceland to the Denmark Strait. This current has sufficient volume transport and continuity on longer timescales to account for a major part of the DSO. A branch of the EGC flowing through the Iceland Sea would support both findings (MACRANDER, 2004).

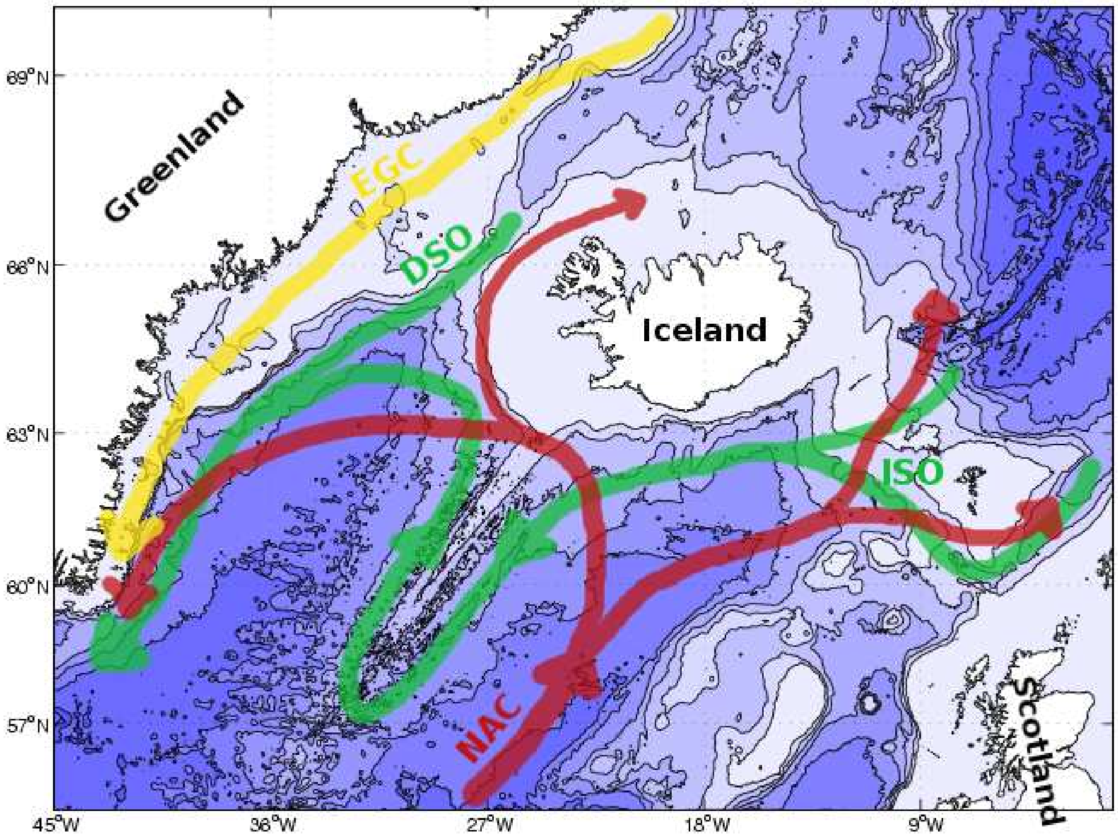

Figure 2.1: *Scheme of the general circulation across the Greenland-Scotland Ridge following* Hansen and Østerhus *(2000). At the surface, branches of the warm and saline North Atlantic Current (NAC) enter the Nordic Seas across the GSR. The East Greenland Current (EGC) transports cold and fresh surface water to the southwest along the Greenland shelf. The Iceland-Scotland overflow water (ISOW) circulates around the Reykjanes Ridge into the Irminger Sea where it joins the Denmark Strait Overflow (DSO). Bathymetry from* Smith and Sandwell *(1997).*

The main driving mechanism for the DSO is the density contrast between the dense source waters and the downstream reservoir (Macrander, 2004), but atmospheric forcing also contributes to driving the overflow (Biastoch et al., 2003). Under the influence of the Coriolis force, the overflow is banked against the Greenland shelf slope as it flows to the southwest. Bottom and interfacial stresses lead to a descent of the overflow plume (Girton and Sanford, 2003). The descent can be seen from the depth of the plume core. At the Denmark Strait sill the centre of the overflow plume is located above the sill depth of $\sim$600 m. 500 km southwest of the sill it is located at around 2000 m depth (Dickson and Brown, 1994).

The first current measurements at the Denmark Strait sill, performed by Worthington (1969), revealed current velocities as high as 1.4 $^{\mathrm{m}}/_{\mathrm{s}}$. The mean speed was slightly above 0.2 $^{\mathrm{m}}/_{\mathrm{s}}$, but many records exceeded 1 $^{\mathrm{m}}/_{\mathrm{s}}$. These findings were supported by later current measurements (Macrander, 2004). The overflow plume encounters steep topography downstream of the sill and the mean plume speed reaches a maximum of 0.6 m/s at 125 km downstream of the sill (GIRTON AND SANFORD, 2003). At a downstream distance of 500 km, the highest mean speeds are around 0.2 m/s (DICKSON AND BROWN (1994), section 4.1 of this thesis).

Transport estimates[3] from current measurements at the sill showed stable transports of 2.7–2.9 Sv (DICKSON AND BROWN, 1994). In recent current measurements MACRANDER ET AL. (2005) found transports decreasing at the sill from 3.7 Sv in 1999 to 3.0 Sv in 2003. The maximum in 1999 correlates with transport calculations from the Angmagssalik mooring array downstream of the sill (ASOF-W, 2006). In the Angmagssalik array, the transport estimates range from 4.0 Sv for water with $\sigma_\theta \geq 27.85$ (ASOF-W, 2006) to 10.7 Sv for water with $\sigma_\theta \geq 27.80$ (DICKSON AND BROWN, 1994). The latter transport estimate includes watermasses from the Iceland-Scotland Overflow that circulate around the Reykjanes Ridge and through the Irminger Sea before they encounter the DSOW (Fig. 2.1). The transport signal in the Angmagssalik array shows no significant trend (ASOF-W, 2006). For comparison, in the Faroe Bank Channel, where a long record of hydrographic and current measurements exists, a decrease in transport by 20% since 1950 was reported by HANSEN ET AL. (2001).

The transports at the sill and in the Angmagssalik array are not steady but variable on transient time-scales. In hydrographic sections close to the sill, the overflow plume appears as propagating domes of cold water (GIRTON AND SANFORD, 2003). This pulsating structure of the plume seems to survive all the way from the sill to the Angmagssalik array (see chapter 4.1).

The structure of the overflow is mainly barotropic at the sill, i. e. the outflow has approximately the same velocity over the whole water column. This changes to a bottom-trapped baroclinic flow downstream of the sill (KÄSE ET AL., 2003). Here the plume has the strongest velocities close to the bottom while the ambient water above is almost at rest.

2.2 Eddies in the overflow

A dominant feature of the DSO is the meso-scale variability observed both in the dense bottom current and at the surface. The breakup of the overflow current into subplumes is connected to the generation of eddies that reach through the whole water column up to the surface.

2.2.1 Observation of eddies in the DSO

BRUCE (1995) observed numerous cold cyclonic eddies in satellite infrared imagery. The eddies, seen at the sea surface, travel along the break of the East Greenland

---

[3] Transport denotes a volume flux throughout this thesis.

Shelf above the path of the overflow plume (Fig. 2.2). The strong thermal front at the eastern edge of the East Greenland Current (EGC) is disturbed by the eddies and therefore visible as spiral structures. A comparison with deep current measurements suggests that the eddies observed at the surface are connected to the density current at the bottom. A study with satellite-tracked drifters by KRAUSS (1996) supports the picture of a chain of cyclonic eddies on the continental slope. The drifters follow the path of the overflow plume and exhibit cyclonic motions. The infrared imagery of the surface front was compared with shipboard temperature measurements by GIRTON AND SANFORD (2003). They find that the locations of the eddy centres move offshore more slowly than the centre of mass of the overflow plume. The surface eddies are enhanced at 125 km downstream while near-surface cyclonic features originate from the sill (GIRTON AND SANFORD, 2003).

KÄSE ET AL. (2003) show a correlation between low sea surface height and high plume thickness. The barotropic currents in the eddies are connected with a slope of the sea surface due to geostrophy.

The main characteristics of the observed meso-scale eddies are listed in table 2.2.1.

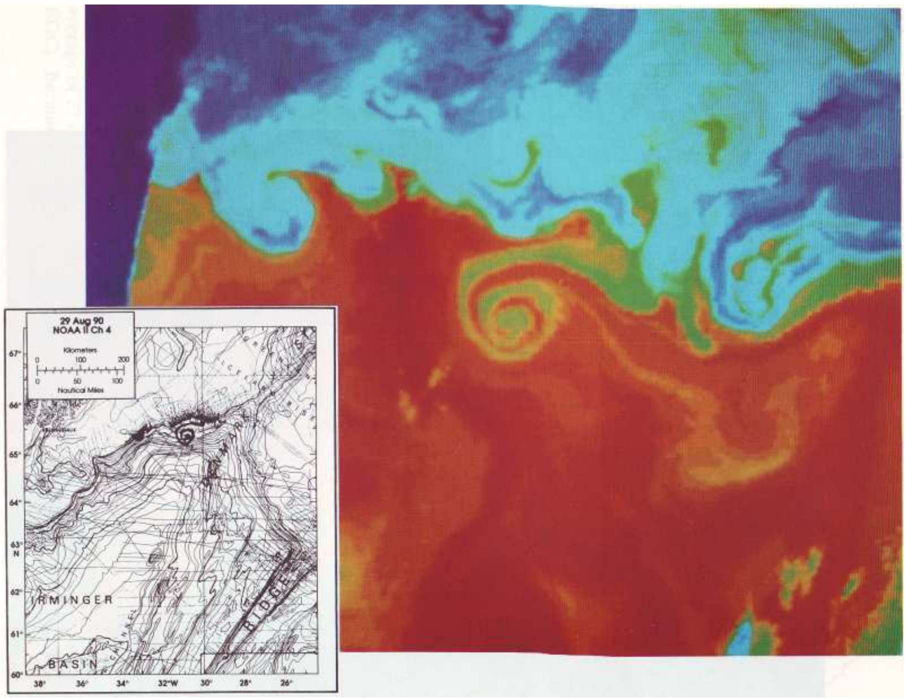

Figure 2.2: *Infrared image of surface eddy signature (*BRUCE*, 1995). The boundary between cold waters in the EGC and warm waters from the North Atlantic Current forms a strong thermal front above the Greenland continental slope. The perturbation of the front at the eastern edge of the EGC makes the eddies visible as a spiral structure. The inset to the lower left shows the position of the vortices on the continental slope.*

Table 2.1: *Characteristics of observed meso-scale eddies (partly adopted from* Spall and Price *(1998)).*

Period: Close to the sill between 1.5 and 2 days (Smith, 1976). The period increases to several days downstream (Dickson and Brown, 1994).

Eddy diameter: Mean eddy diameter 34 km, typical diameters 20–40 km (Bruce, 1995).

Distance: Mean distance between two eddies is 54 km (Bruce, 1995).

Eddy propagation rate: 27 $^{\mathrm{cm}}/_{\mathrm{s}}$ (Bruce, 1995). Girton (2001) finds eddy propagation rates that compare well with the mean plume speed on the initial 300 km.

Azimuthal speed: Eddies are in solid body rotation, the mean speed at 10 km distance from the eddy core is above 30 $^{\mathrm{cm}}/_{\mathrm{s}}$ (Krauss, 1996).

Vertical structure: Maximum eddy kinetic energy at the interface between DSOW and ambient water (Dickson and Brown (1994), Krauss (1996)).

Vorticity: The strongest surface eddies are cyclones (Bruce (1995), Girton (2001)).

Reach: Eddies are located as far south as $62^\circ\,50'\,\mathrm{N}$ (Bruce, 1995).

2.2.2 Physical mechanisms for eddy generation

Theories that explain the observed meso-scale eddies in the DSO are based on the physical mechanisms of vortex stretching and baroclinic instability. In order to gain a deeper insight into the eddy formation process, these two principles are presented in this section along with topographic waves that are important when baroclinic instability is addressed.

Vortex stretching The vorticity of a water parcel can be split into two parts. The rotation of the earth leads to the planetary vorticity f

$$f = 2\Omega \sin\phi \tag{2.1}$$

with earth rotation rate Ω and latitude ϕ. The relative vorticity ξ is defined as the curl of the horizontal velocity field $\boldsymbol{v}(u, v, w)$:

$$\xi = \boldsymbol{\nabla} \times \boldsymbol{v} = \frac{\partial v}{\partial x} - \frac{\partial u}{\partial y}. \tag{2.2}$$

The sum of planetary and relative vorticity is the absolute vorticity. The absolute vorticity divided by the height of the water layer H is called the potential vorticity q:

$$q = \frac{f + \xi}{H}. \tag{2.3}$$

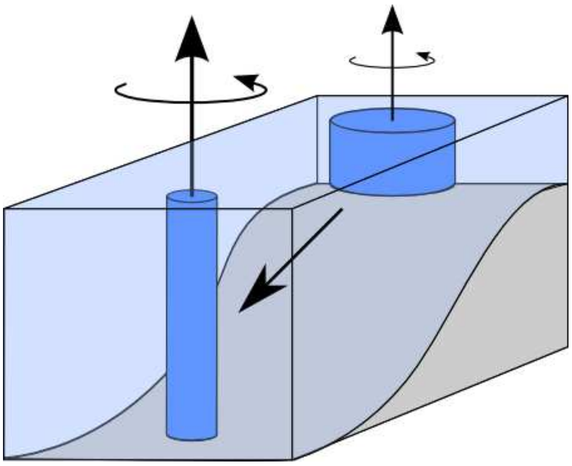

Figure 2.3: *The vortex stretching mechanism. As the water column is moved into deeper water, it is stretched and changes its moment of inertia. The result is a gain in relative vorticity.*

The potential vorticity q is a conserved quantity for an inviscid flow. A water column that moves into deeper water is stretched because of volume conservation (assuming constant density) as depicted in Fig. 2.3. When this happens at a constant latitude ϕ or over a small horizontal distance with negligible change in f, the increase in height H must be balanced by an increase in relative vorticity.

The gain of relative vorticity of a stretched water column can also be understood as follows: As the water column is stretched because of volume conservation, the radius of the column decreases. This leads to a decrease in moment of inertia. If the flow is inviscid, rotational energy is conserved and the water column has to spin faster in order to balance the change in moment of inertia.

Topographic waves A consequence of the conservation of potential vorticity is the existence of waves that propagate along isobaths. A water parcel which is moved over deeper ground is stretched and gains cyclonic vorticity. This acts as a restoring force which moves the water parcel back to its original depth and beyond into shallower water. There the parcel is squeezed and gains anticyclonic vorticity which again acts as a restoring force.

Baroclinic instability A baroclinic geostrophic flow, i. e. an inviscid flow under the influence of earth rotation with a vertical shear, is necessarily accompanied by a sloping isopycnal (Fig. 2.4). This follows from the thermal wind equation (v is horizontal velocity, f Coriolis parameter and ρ density)

$$\frac{\partial v}{\partial z} = -\frac{g}{\rho_0 f}\frac{\partial \rho}{\partial x}, \tag{2.4}$$

which states that a vertical shear in velocity can only be supported by a horizontal density gradient and vice versa.

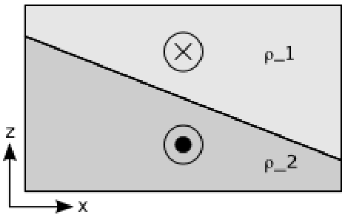

Figure 2.4: *A baroclinic geostrophic flow accompanied by a tilted interface. The sloping isopycnal generates the horizontal pressure gradient needed for geostrophic equilibrium.*

The system with a sloping interface has higher potential and kinetic energy than a system of two fluids with a horizontal interface. This is because the centre of gravity is not in the lowest position and the horizontal pressure gradient maintains the flow field. The favourable state of rest would be the one with zero kinetic energy and lowest potential energy, hence with a horizontal isopycnal. A simple and direct relaxation of the system is not possible. The tilting of the sloping isopycnal into a horizontal position squeezes and stretches the watercolumns. This produces relative vorticity since potential vorticity is conserved when friction is neglected. Under certain conditions, the vortices resulting from a small perturbation may grow and perturb the system even more. The flow then becomes unstable and evolves away from its original state. In this process, the potential energy associated with the sloping isopycnal is transferred into kinetic energy of the perturbations.

Two criteria have to be matched for a perturbation to grow. One criterion is a phase difference between perturbations in the upper and lower layer of about $^{\pi}/_{4}$ (see Fig. 2.5 for further explanation). This criterion is reflected in the name of the process, the perturbation must be baroclinic to induce the instability. The other criterion is the wavelength of the perturbation. The wavelength has to be of the same order of size as the Rossby deformation radius[4]. In linear theory, CUSHMAN-ROISIN (1994) calculates the most unstable wavelength to approximately four times the Rossby radius. The Rossby radius for the DS sill is estimated between 11 km (KÄSE AND OSCHLIES, 2000) and 14 km (WHITEHEAD, 1998). Hence, it is possible that the observed eddies result from a baroclinic instability (compare values in table 2.2.1).

2.2.3 Numerical studies on eddies in the DSO

A number of numerical studies have been performed to investigate the eddy generation mechanism in the DSO and its underlying physical processes.

The first attempt was a steady streamtube model by SMITH (1976). Referring to baroclinic instabilities he found the model to be unstable at a wavelength of 80 km and a period of 2.1 days. This agrees with peaks in current meter spectra. Observations also reveal a cross-stream perturbation heat flux that reduces the potential energy associated with the sloping isotherm and feeds the instabilities. AAGAARD

---

[4] The Rossby deformation radius gives the length scale at which rotational effects become important. It is defined as $Ro = \frac{\sqrt{g'H}}{f}$ where $g' = g\frac{\Delta\rho}{\rho}$ is the reduced density and H is the depth of the water layer.

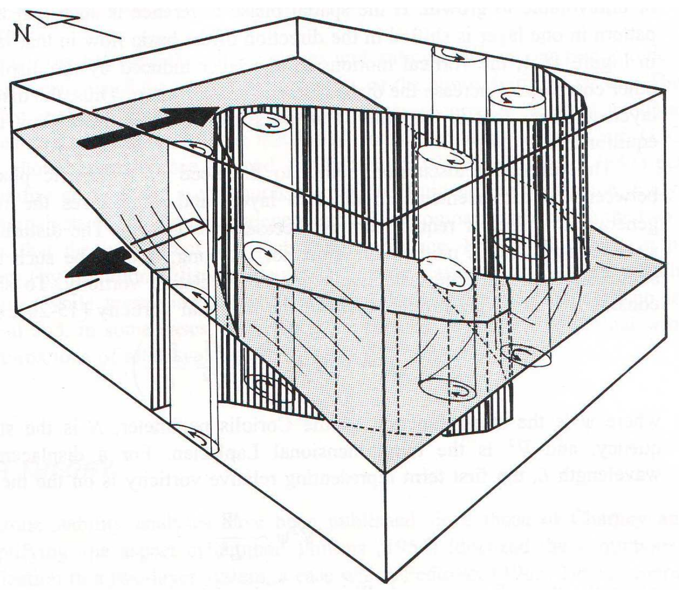

Figure 2.5: *Schematic view of the growing process of a baroclinic instability. The thick black arrows indicate the shear flow with the tilted interface. A water column in the upper layer moved over shallow water by a perturbation is squeezed and gains anticyclonic vorticity. Other than a solid bottom, the interface can slacken a little so that the lower water column is squeezed as well. Hence, the whole water column gains anticyclonic vorticity. Over deeper water the same process takes place with opposite sign. The slackening of the interface both over shallow and deep water is in the direction of a potential energy release. Hence, potential energy associated with the sloping interface is transferred into kinetic energy of the vortices. Since the generated vortices are located at the maxima of the perturbation wave, they do not lead to growth of the disturbance. Only the interplay with a perturbation wave in the lower layer that is in quadrature with the upper one, inducing the same stretching and squeezing mechanism, can lead to growth of the perturbations. From* Cushman-Roisin *(1994).*

and Malmberg (1978) also suggest baroclinic instabilities to account for the high variability. However, the unstable frequency band is found to be highly variable itself and they cannot demonstrate a relationship between this variability and the bulk flow parameters.

If the source for the variability were exclusively baroclinic instability, the same number of cyclones and anticyclones should occur. This contradicts the observations of Bruce (1995) who found predominantly cyclones. Numerical simulations of Krauss and Käse (1998) reveal a strong nonlinear nature of the eddies, they can not be explained by simple linear wave theory.

In 3D simulations of Jiang and Garwood (1996), baroclinic instabilities together with bottom friction lead to the breakup into subplumes at the offshore side of the plume. The instabilities are manifested as topographic Rossby waves. The water column over the subplumes is stretched additionally. Vortex stretching then leads to the formation of cyclonic eddies. The comparable model of Krauss and

Käse (1998) with different inflow boundary conditions produces anticyclonic vortices on the upper slope of the shelf in addition to the cyclones. The anticyclones are produced by squeezing of water columns. The small downslope movement of the eddies as they travel southward amplifies the cyclonic vortices and weakens anticyclones due to increasing water depth.

In Denmark Strait the currents have a strong barotropic component. In the EGC the near surface Polar water, the Arctic Intermediate Water (AIW) at intermediate depths and the DSOW at the bottom all flow to the south. This is different to the exchanges through Faroe Bank Channel (FBC) and Strait of Gibraltar, where a current reversal exists at intermediate depths. The outflow in all water layers caused Spall and Price (1998) to develop the potential vorticity (PV) outflow hypothesis. They argue that the intermediate layer is stretched as it flows into the Irminger Sea while the EGC and the DSOW need no stretching. The dominant eddy generation process is an adjustment of the high PV outflow water column to the low PV oceanic environment.

In simulations run by Jungclaus et al. (2001), perturbations exceeding a certain cutoff wavelength lead to baroclinic instability and both cyclones and anticyclones are formed. The dominance of cyclones is then explained with PV arguments.

Girton (2001) concludes that baroclinic and possibly also barotropic instabilities[5] occur as the flow approaches the sill. These instabilities generate eddies with small amplitudes. Further downstream where the overflow descents, the cyclonic eddies are intensified through vortex stretching (see Fig. 2.6 for a sketch of these processes).

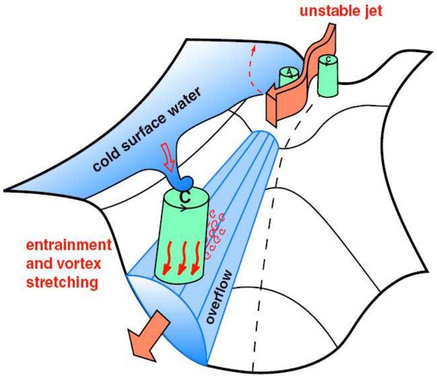

Figure 2.6: *Sketch of the processes that generate the surface eddies observed in infrared imagery (Girton, 2001).*

---

[5] Barotropic instabilities evolve from a horizontal shear in velocity. They receive their energy from the kinetic energy of the flow.

2.2.4 Laboratory experiments on eddy generation in dense overflows

The descent of dense water on a sloping bottom has been simulated in laboratory studies with rotating tanks. These tank experiments provide a mean to study the eddy formation process in a dense current under idealised conditions. In this section, four of the experiments that closely resemble the DSO are briefly presented. The experimental setup of the four studies differs only gradually as all use a plain sloping bottom with resting and, except for one case, unstratified ambient water (Fig. 2.7). Nevertheless, different source design (e.g. inflow parallel or perpendicular to the slope) and parameter ranges might lead to different mechanisms for eddy generation.

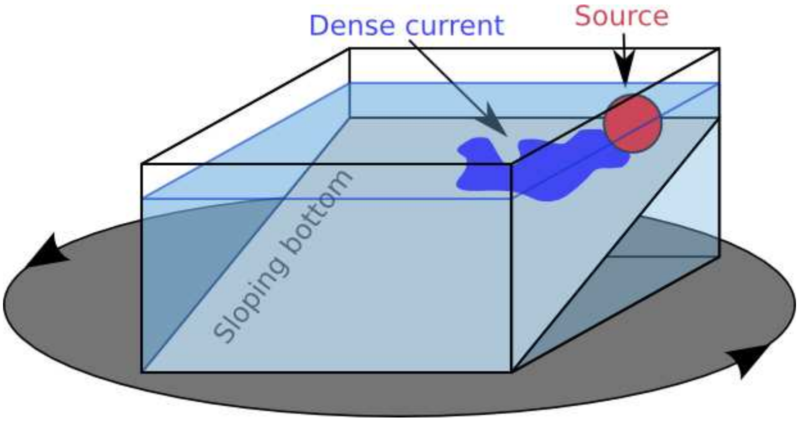

Figure 2.7: *Generalised sketch of tank experiments setup. The source for the dense water spilled on the sloping bottom may be a nozzle or the flow over a weir.*

Strong cyclonic vortices form in the ambient fluid above the overflow for certain parameter ranges in each experiment. This causes the dense current to break up into a series of domes. For positive planetary vorticity f (northern hemisphere), the vortices travel with the shallow water on the right hand side until they reach the wall of the tank.

WHITEHEAD ET AL. (1990) observe eddies for strong jets inserted close to the coast, i.e. with a thin overlying layer of ambient fluid. The eddies travel close to the coast while downslope in the bottom layer roll waves develop. These waves are present even in the cases without vortex formation. WHITEHEAD ET AL. (1990) suggest the eddies to be generated by entrainment through small-scale mixing of fresh water into the dense current. Sinking of the mixed water into the dense current produces the cyclonic vortex in the upper layer. The sinking can be understood as stretching of the water column, hence the eddies are generated through vortex stretching as explained in section 2.2.2.

LANE-SERFF AND BAINES (2000) describe the vortex formation process as the stretching of the upper-layer fluid after it is drawn away from the coast by the dense current. In addition, continuous viscous draining from the current also causes stretching in the upper ambient fluid. The vortices then develop through vortex stretching. The comparison between unstratified ambient water and a stratified environment shows that the stratified ambient water leads to stronger, more frequent eddies.

ETLING ET AL. (2000) identify two regimes of vortex formation. In strong density currents with weak rotation the vortices are formed by stretching of the upper layer near the source. For weak currents and strong rotation the vortex formation is found to be due to a baroclinic instability of the bottom plume. As in the numerical model of JIANG AND GARWOOD (1996), the instability is manifested as growing topographic Rossby waves. For a characterisation of the two flow regimes an interaction parameter is introduced. It is based on the height of the dense fluid, the bottom slope and the Rossby deformation radius which in turn depends on the height of the above fluid layer. The interaction parameter of the 'real' DS is in the transition between the two regimes. A comparison of the eddy formation period in experiment and DSO suggests that the barotropic mechanism of vortex stretching is more likely the process to produce eddies in the DSO than the baroclinic instability.

CENEDESE ET AL. (2003) observe three different flow regimes: A laminar flow, a wave regime similar to the roll waves in WHITEHEAD ET AL. (1990) and an eddy regime. The regimes are found to be dependent on Ekman number[6] and Froude number[7]. Small Ekman numbers indicate that rotational motion can overcome friction, hence eddies can evolve. When the Froude number is larger than one, perturbations cannot travel upstream anymore. A wave regime with waves travelling downstream is more likely to happen. Fig. 2.8 shows a diagram with the dependence of the regimes on Ekman number and Froude number. The observed eddy regime is qualitatively similar to LANE-SERFF AND BAINES (2000) and ETLING ET AL. (2000).

The tank experiments described above reflect the complexity of the eddy formation process in the DSO. The majority of the experiments suggest the vortex stretching mechanism to be the primary process. Nevertheless, as can be seen in ETLING ET AL. (2000), there is a smooth transition to an eddy regime induced by baroclinic instability.

The laboratory studies with highly idealised topographic setup and different source designs generate cyclonic eddies and the breakup of the dense current for a wide range of parameters. This leads to the valuable conclusion that the vortex formation over dense currents flowing down a sloping bottom is not only a coincidence of certain parameters but more an inherent characteristic over a wider range of parameters.

---

[6] The Ekman number gives the ratio of viscous forces to the forces arising from planetary rotation. It is defined as $Ek = \frac{\nu}{\Omega H^2}$ with the viscosity ν, ambient rotation rate Ω and water depth H.

[7] The Froude number is a measure for the importance of stratification. It is dimensionless. It is defined as $Fr = \frac{U}{\sqrt{g'H}}$ where U is the horizontal velocity, g' reduced density and H water depth. The denominator is the gravity wave speed. When $Fr \geq 1$, the velocity is higher than the gravity wave speed and no information can travel upstream.

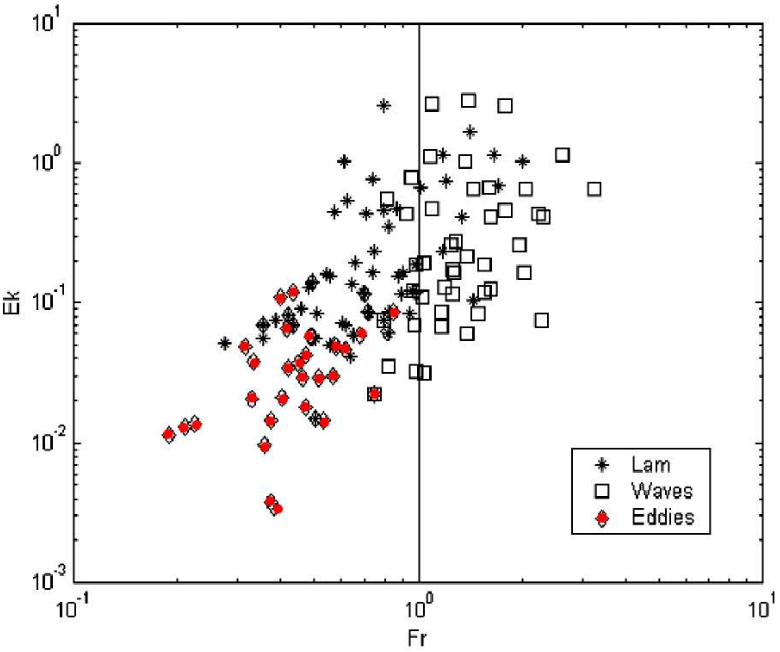

Figure 2.8: *Diagram of* CENEDESE ET AL. *(2003) for different flow regimes. Eddies (marked red) are found for small Ekman numbers and values of the Froude number smaller than unity.*

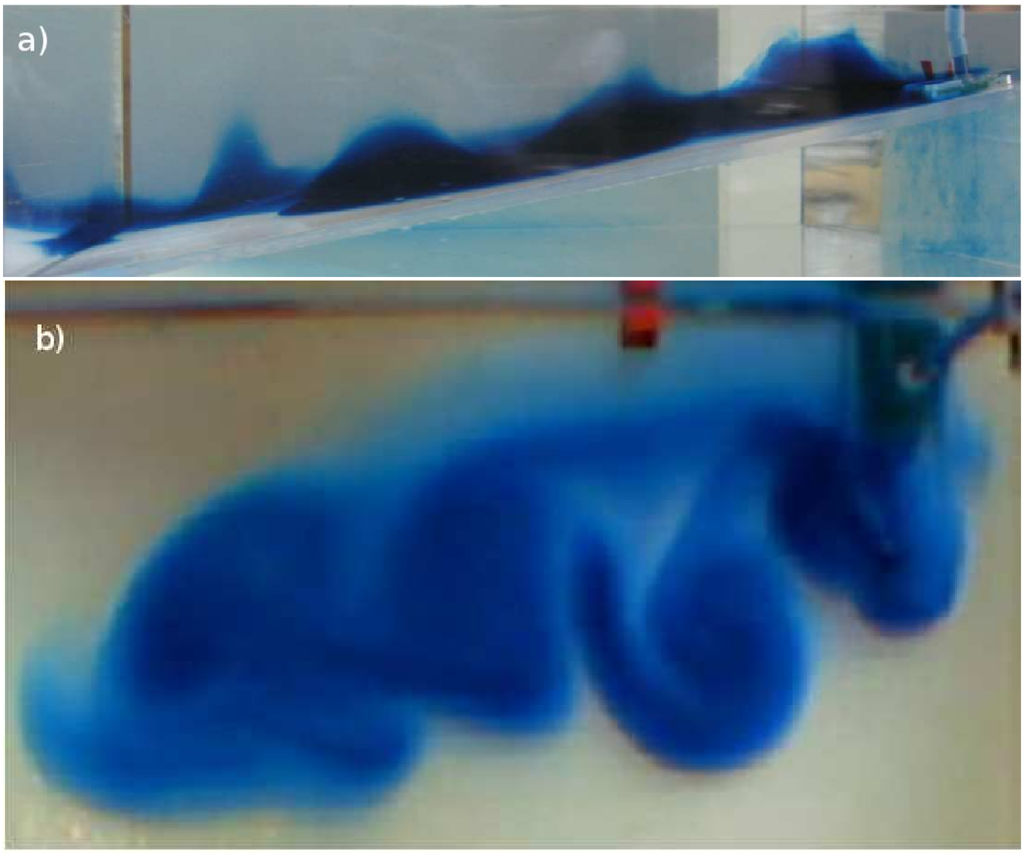

Figure 2.9: *Side view (a) and top view (b) of a rotating tank experiment with a dense current on a sloping bottom. The dense water is dyed with blue food colour to make it visible in the experiment. The dense water source is located to the upper right in both views. Eddies are formed as the dense water descends on the slope. The thickness of the dense water layer increases below the eddies. The photos are a product of the workshop* Tankexperimente und Simulation von dynamischen Prozessen *held at the* Institut für Meereskunde, Universität Hamburg *in summer 2006.*

2.3 Mixing and entrainment

The volume increase of the dense overflow current by mixing ambient water into the plume is termed entrainment. Entrainment processes almost double the transport of the DSO within the first 500 km from the sill (Dickson and Brown, 1994) and hence influence the final characteristics of the North Atlantic Deep Water (NADW). The major factor controlling the density contrast between overflow and ambient water is the temperature (Girton and Sanford, 2003). Thus, the mixing process is considered to be solely an exchange of heat in this study. This section gives a theoretical introduction to the exchange of heat on molecular and turbulent levels. Past studies on entrainment in the DSO are presented.

2.3.1 The equation of heat conduction

A general conservation law for field functions is presented and used to derive the equation of continuity and the law of energy conservation. The equation of heat flux is derived. It is identical with the first law of thermodynamics. A simplification of this equation leads to the equation of heat conduction. The derivations presented here closely follow Krauss (1973) and use Kundu (1990) where further explanation is needed.

A general conservation law for field functions Let ψ be a property of a fluid per unit mass. The total amount of ψ in a volume V at a fixed position with density ρ is

$$\int_V \psi \rho dV. \tag{2.5}$$

There are two ways for the amount of ψ in V to change. The property ψ can be transported across the surface S of the volume V with the fluid velocity $\boldsymbol{v}$ or external forces create a source density q_ψ in the volume. The general conservation law for ψ then reads

$$\int_V \frac{\partial \psi \rho}{\partial t} dV = -\int_S \psi \rho \boldsymbol{v} d\boldsymbol{S} + \int_V q_\psi dV. \tag{2.6}$$

The surface integral term may be rewritten using the Gaussian theorem[8]:

$$\int_V \frac{\partial \psi \rho}{\partial t} dV = -\int_V \nabla \cdot \psi \rho \boldsymbol{v} dV + \int_V q_\psi dV \tag{2.7}$$

Since the integration volume V is arbitrary in size and shape, the equation holds without integration:

$$\frac{\partial \psi \rho}{\partial t} = -\nabla \cdot \psi \rho \boldsymbol{v} + q_\psi \tag{2.8}$$

---

[8] The relation $\int_V \nabla \cdot \boldsymbol{v} dV = \int_S \boldsymbol{v} dS$ is called the Gaussian integral theorem. In this form, it states that the divergence of the velocity field is proportional to the volume flux through the surface of the volume.

The equation of continuity The equation of continuity is the hydrodynamic form of the mass conservation law. It can easily be derived from the general conservation law (eq. 2.8). The source term q_ψ is zero since external influences cannot produce mass in the volume. The property ψ is taken to be the specific mass, i. e. mass per unit mass: $\psi = 1$. This leads to

$$\frac{\partial \rho}{\partial t} + \nabla \cdot \rho \boldsymbol{v} = 0. \tag{2.9}$$

With $\nabla \cdot \rho \boldsymbol{v} = \rho \nabla \cdot \boldsymbol{v} + \boldsymbol{v} \nabla \cdot \rho$ and the total time derivative[9] of ρ, the equation of continuity reads

$$\frac{1}{\rho}\frac{d\rho}{dt} + \nabla \cdot \boldsymbol{v} = 0. \tag{2.10}$$

The law of energy conservation The general conservation law (eq. 2.6) can be used to derive an energy conservation law. For this purpose, ψ is chosen to be the total energy. The total energy is the sum of kinetic and internal energy e per unit mass, $\psi = \boldsymbol{v}^2/2 + e$. The potential energy is included in the energy production term q_ψ as the work of the gravity field on the liquid element. Energy can be generated in the volume by work applied at the surface of the volume, inside the volume or by a heat flux across the surface. When sources of heat and radiation are ignored, the generation of energy q_ψ in a stationary volume consists of:

1. The work done by the volume-proportional forces $\boldsymbol{k}$, $\int_V \boldsymbol{v} \cdot \boldsymbol{k} dV$. The volume-proportional forces include the gravity and tidal forces. With their potentials ϕ and ϕ_G, $\boldsymbol{k} = -\rho(\nabla \phi + \nabla_h \phi_G)$.
2. The work done by the surface forces, $\int_S (\boldsymbol{v} \cdot \Pi) d\boldsymbol{S}$. The stress tensor Π is symmetrical. It can be split up into $\Pi = -pI + \overset{\circ}{\Pi}$, i. e. into the sum of pressure times the unity vector and the frictional tensor.
3. The heat flux $-\int_S \boldsymbol{H} \cdot d\boldsymbol{S}$.

With these terms, the energy conservation law in integral form is

$$\begin{aligned} &\int_V \frac{\partial}{\partial t} \rho \left(\frac{\boldsymbol{v}^2}{2} + e \right) = \\ &= - \int_S \rho \left(\frac{\boldsymbol{v}^2}{2} + e \right) \boldsymbol{v} \cdot d\boldsymbol{S} + \int_V \boldsymbol{v} \cdot \boldsymbol{k} dV + \int_S (\boldsymbol{v} \cdot \Pi) \cdot d\boldsymbol{S} - \int_S \boldsymbol{H} \cdot d\boldsymbol{S}. \end{aligned} \tag{2.11}$$

It is worth to note that the energy conservation law is consistent with the first law of thermodynamics. For a material volume, i. e. for a volume following the flow,

---

[9] The total time derivative $\frac{d\psi}{dt} = \frac{\partial \psi}{\partial t} + \boldsymbol{v} \nabla \psi$ is the sum of the local derivative and the advective term.

it states that the change of stored energy equals the sum of work done and heat addition to the material volume. If a fixed volume is chosen, advective terms as in eq. 2.11 have to be included.

The Gaussian theorem can be applied here as in eq. 2.7. Again, the equation must hold without integration since the integration volume is arbitrary:

$$\frac{\partial}{\partial t}\rho\left(\frac{\boldsymbol{v}^2}{2}+e\right) = -\nabla\cdot\left[\rho\left(\frac{\boldsymbol{v}^2}{2}+e\right)\cdot\boldsymbol{v}-\boldsymbol{v}\cdot\Pi+\boldsymbol{H}\right]+\boldsymbol{v}\cdot\boldsymbol{k}. \tag{2.12}$$

Splitting up the stress tensor into a pressure term and a frictional tensor leads to the energy conservation law in differential form:

$$\frac{\partial}{\partial t}\rho\left(\frac{\boldsymbol{v}^2}{2}+e\right) = -\nabla\cdot\left[\rho\left(\frac{\boldsymbol{v}^2}{2}+e\right)\cdot\boldsymbol{v}-\boldsymbol{v}\cdot\overset{\circ}{\Pi}+\boldsymbol{H}\right]-\boldsymbol{v}\cdot\nabla p-p\nabla\cdot\boldsymbol{v}+\boldsymbol{v}\cdot\boldsymbol{k}. \tag{2.13}$$

The energy conservation law states that the energy in the volume element is changed by:

- The divergence of the energy flux which consists of an energy flux due to the velocity $\boldsymbol{v}$, an energy flux due to internal friction and a heat flux $\boldsymbol{H}$.
- The work by the surrounding pressure field on the volume element.
- A compression term.
- The work done by gravity and tidal forces.

The equation of heat flux A conservation law for the internal energy can be obtained by the subtraction of the hydrodynamic equation of motion from the energy conservation law. The hydrodynamic equation of motion reads[10]

$$\rho\left(\frac{\partial\boldsymbol{v}}{\partial t}+\boldsymbol{v}\cdot\nabla\boldsymbol{v}\right) = \boldsymbol{k}-\nabla p+\nabla\cdot\overset{\circ}{\Pi}. \tag{2.14}$$

Scalar multiplication of this equation with $\boldsymbol{v}$ yields an equation that can be subtracted from the energy conservation law:

$$\rho\boldsymbol{v}\cdot\frac{\partial\boldsymbol{v}}{\partial t}+\boldsymbol{v}\cdot(\boldsymbol{v}\cdot\nabla\boldsymbol{v}) = \boldsymbol{v}\cdot\boldsymbol{k}-\boldsymbol{v}\cdot\nabla p+\boldsymbol{v}\cdot\nabla\cdot\overset{\circ}{\Pi}. \tag{2.15}$$

The left hand side can be rewritten using the relations $\rho\boldsymbol{v}\cdot\frac{\partial\boldsymbol{v}}{\partial t}=\frac{\partial}{\partial t}\frac{\rho\boldsymbol{v}^2}{2}-\frac{\boldsymbol{v}^2}{2}\frac{\partial\rho}{\partial t}$ and $\boldsymbol{v}\cdot(\boldsymbol{v}\cdot\nabla\boldsymbol{v})=\boldsymbol{v}\nabla\frac{\boldsymbol{v}^2}{2}$:

$$\rho\boldsymbol{v}\cdot\frac{\partial\boldsymbol{v}}{\partial t}+\boldsymbol{v}\cdot(\boldsymbol{v}\cdot\nabla\boldsymbol{v}) = \frac{\partial}{\partial t}\frac{\rho\boldsymbol{v}^2}{2}-\frac{\boldsymbol{v}^2}{2}\frac{\partial\rho}{\partial t}+\rho\boldsymbol{v}\cdot\nabla\frac{\boldsymbol{v}^2}{2}. \tag{2.16}$$

---

[10] For a derivation of the hydrodynamic equation of motion see e. g. KRAUSS (1973)

The continuity equation (2.9) provides $\frac{\partial \rho}{\partial t} = -\nabla \rho \boldsymbol{v}$. The last two terms in eq. 2.16 combine to $\nabla \cdot \left(\frac{\boldsymbol{v}^2}{2} \cdot \rho \boldsymbol{v} \right)$. Finally, the scalar product of hydrodynamic equation and $\boldsymbol{v}$ reads

$$\frac{\partial}{\partial t} \frac{\rho \boldsymbol{v}^2}{2} = -\nabla \cdot \left(\frac{\boldsymbol{v}^2}{2} \cdot \rho \boldsymbol{v} \right) + \boldsymbol{v} \cdot \boldsymbol{k} - \boldsymbol{v} \cdot \nabla p + \boldsymbol{v} \cdot \nabla \cdot \overset{\circ}{\Pi}. \tag{2.17}$$

Substraction of eq. 2.17 from the energy conservation law (2.13) yields a conservation law for the internal energy:

$$\frac{\partial \rho e}{\partial t} = -\nabla \cdot (\rho e \boldsymbol{v}) - \nabla \cdot \boldsymbol{H} - p \nabla \cdot \boldsymbol{v} + \nabla \boldsymbol{v} \cdot \cdot \overset{\circ}{\Pi}. \tag{2.18}$$

It was used here that $\nabla \cdot (\overset{\circ}{\Pi} \cdot \boldsymbol{v}) = (\nabla \cdot \overset{\circ}{\Pi}) \cdot \boldsymbol{v} + \nabla \boldsymbol{v} \cdot \cdot \overset{\circ}{\Pi}$, where $\cdot\cdot$ means double scalar multiplication. Eq. 2.18 states that the internal energy is changed by

- convective and molecular heat flux (first two terms);
- compression and
- energy dissipation due to internal friction.

Applying the product rule in the two terms including the internal energy e and rearranging the terms yields

$$\rho \left(\frac{\partial e}{\partial t} + \boldsymbol{v} \cdot \nabla e \right) + e \left(\frac{\partial \rho}{\partial t} + \nabla \cdot \rho \boldsymbol{v} \right) = \rho \frac{de}{dt}. \tag{2.19}$$

The first bracket is the total time derivative of e (compare footnote on p. 18). The second bracket is the LHS of the continuity equation (2.9) and therefore equal zero. With these simplifications eq. (2.18) reads

$$\frac{de}{dt} = -\frac{1}{\rho} \left(\nabla \cdot \boldsymbol{H} + p \nabla \cdot \boldsymbol{v} - \nabla \boldsymbol{v} \cdot \cdot \overset{\circ}{\Pi} \right). \tag{2.20}$$

This equation is identical to the first law of thermodynamics. The heat supply dQ/dt is the sum of viscous dissipation and heat flux:

$$\frac{dQ}{dt} = \frac{1}{\rho} \left(\nabla \boldsymbol{v} \cdot \cdot \overset{\circ}{\Pi} - \nabla \cdot \boldsymbol{H} \right). \tag{2.21}$$

The equation of continuity (2.10) can be rewritten by replacing density with the specific volume α:

$$\nabla \cdot \boldsymbol{v} = -\frac{1}{\rho} \frac{d\rho}{dt} = \frac{1}{\alpha} \frac{d\alpha}{dt}. \tag{2.22}$$

Then eq. (2.20) takes the form of the first law of thermodynamics:

$$\frac{dQ}{dt} = \frac{de}{dt} + p \frac{d\alpha}{dt}. \tag{2.23}$$

If the heat flux $\boldsymbol{H}$ obeys the Fourier law

$$\boldsymbol{H} = -k\nabla T, \tag{2.24}$$

with k being a constant, the conservation law for the internal energy, also called equation of heat flux, reads

$$\frac{de}{dt} = \frac{1}{\rho}\left(k\nabla^2 T - p\nabla\cdot\boldsymbol{v} + \nabla\boldsymbol{v}\cdot\cdot\overset{\circ}{\Pi}\right). \tag{2.25}$$

The Boussinesq approximation The Boussinesq approximation states that density differences are sufficiently small to be neglected except for terms involving gravity. The continuity equation (2.10) reduces to the incompressible form

$$\nabla\cdot\boldsymbol{v} = 0 \tag{2.26}$$

in this approximation. In other words, the magnitude of $\rho^{-1}(d\rho/dt)$ is small in comparison to the magnitude of the velocity gradients $\nabla\cdot\boldsymbol{v}$.

The equation of heat conduction A simple equation of heat conduction can be obtained when the Boussinesq approximation is applied to the equation of heat flux (2.25). The compression term $p\nabla\cdot\boldsymbol{v}$ vanishes by virtue of the simplified equation of continuity (2.26). Using $e = c_pT$, with c_p being the specific heat capacity at constant pressure, the equation of heat flux (2.25) reduces to

$$\rho c_p\frac{dT}{dt} = k\nabla^2 T + \nabla\boldsymbol{v}\cdot\cdot\overset{\circ}{\Pi}. \tag{2.27}$$

The term involving heating due to viscous dissipation of energy, $\nabla\boldsymbol{v}\cdot\cdot\overset{\circ}{\Pi}$, is very small compared to the LHS of the equation if the Boussinesq approximation applies (KUNDU, 1990). Thus, with the thermal diffusivity $\kappa \equiv k/(\rho c_p)$, the equation of heat conduction reads

$$\frac{dT}{dt} = \kappa\nabla^2 T. \tag{2.28}$$

2.3.2 The averaged heat equation

The mixing process described with the equation of heat conduction (2.28) is solely due to the thermal energy of the molecules. It takes a very long time to be efficient. Mixing can be greatly enhanced when the watermasses are stirred (see Fig. 2.10). The stirring extends the interfaces with temperature gradients over which mixing can occur.

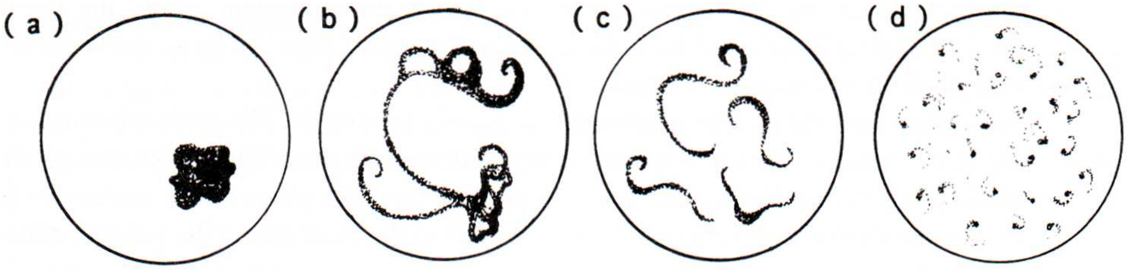

Figure 2.10: *Illustration of enhanced mixing through stirring (*Knauss*, 1997). Imagine the dark area in (a) being a patch of warm water in a bowl with cold water. Progressing from (a) to (d), stirring breaks up the patches of warm water. The number of interfaces with sharp temperature gradients where molecular mixing occurs increases.*

Averaged fields A turbulent heat transport equation can be derived by splitting the fields into mean parts and deviations of these (Krauss, 1973). This implies that turbulent flows may be seen as laminar with a secondary motion superimposed. The mathematical formulation is achieved by dividing the field f into two parts - one part describes the mean characteristics of the field while the other describes the secondary motion:

$$f(t) = \overline{f(t)} + f'(t) \tag{2.29}$$

The mean field $\overline{f(t)}$ is the average value of f over a time interval T at the time t. The secondary field f' is the difference between f and $\overline{f}$. Several relations hold for the two fields:

$$\overline{\overline{f}} = \overline{f}, \quad \overline{f'} = 0, \quad \overline{\overline{f}_1\,\overline{f}_2} = \overline{f}_1\,\overline{f}_2, \quad \overline{\overline{f}_1 f_2'} = 0, \quad \overline{\overline{f}_1 f_2' f_3'} = \overline{f_1' f_2' f_3'} \tag{2.30}$$

The averaged equation of continuity The concept of averaged equations can be used to obtain an averaged form of the continuity equation (2.9). It will be useful later on.

$$\overline{\frac{\partial(\overline{\rho} + \rho')}{\partial t}} + \overline{\nabla(\overline{\rho} + \rho')(\overline{\boldsymbol{u}} + \boldsymbol{u'})} = 0 \tag{2.31}$$

Since deviations in density ρ' are in the order of magnitude 10^{-3} $^{\mathrm{g}}/_{\mathrm{cm}^3}$, terms with ρ' can generally be neglected. Using the third relation in (2.30), the averaged continuity equation is

$$\frac{\partial\overline{\rho}}{\partial t} + \nabla\overline{\rho}\,\overline{\boldsymbol{u}} = 0 \tag{2.32}$$

The averaged heat equation It is useful to rewrite the equation of heat conduction (2.28) using the continuity equation (2.9):

$$\frac{\partial c_p \rho T}{\partial t} = -\nabla(c_p \rho T \boldsymbol{u}) + \nabla(k \nabla T) \tag{2.33}$$

Now the fields are averaged, c_p and k are considered constant:

$$c_p\frac{\partial\overline{(\bar\rho+\rho')(\bar T+T')}}{\partial t} = -c_p\nabla\overline{(\bar\rho+\rho')(\bar{\boldsymbol{u}}+\boldsymbol{u'})(\bar T+T')} + \nabla\overline{(k\nabla(\bar T+T'))} \tag{2.34}$$

Neglecting terms with ρ' and using the relations in (2.30), this reduces to

$$c_p\frac{\partial\bar\rho\bar T}{\partial t} + c_p\nabla(\bar\rho\bar{\boldsymbol{u}}\bar T) = -c_p\nabla(\bar\rho\overline{\boldsymbol{u'}T'}) + \nabla k\nabla\bar T \tag{2.35}$$

The left hand side can be simplified using the averaged equation of continuity (2.32):

$$\begin{aligned}\frac{\partial\bar\rho\bar T}{\partial t} + \nabla(\bar\rho\bar{\boldsymbol{u}}\bar T) &= \bar\rho\frac{\partial\bar T}{\partial t} + \bar T\frac{\partial\bar\rho}{\partial t} + \bar T\underbrace{\nabla(\bar\rho\bar{\boldsymbol{u}})}_{-\frac{\partial\bar\rho}{\partial t}} + \bar\rho\bar{\boldsymbol{u}}\nabla\bar T \\ &= \bar\rho\frac{\partial\bar T}{\partial t} + \bar\rho\bar{\boldsymbol{u}}\nabla\bar T \qquad (2.36)\end{aligned}$$

For the turbulent term on the right hand side of eq. (2.35), an eddy diffusivity can be defined to connect turbulent mixing with the temperature gradient in the same form as the molecular diffusion term (in component notation):

$$c_p\bar\rho\overline{u_i'T'} = -A(i)\frac{\partial T}{\partial x_i} \tag{2.37}$$

The eddy diffusivities for turbulent mixing are several orders of magnitude larger than the molecular diffusion coefficient. Therefore it can be neglected. With the horizontal and vertical gradients and eddy diffusivities ∇_h, A_h and ∇_v, A_v, respectively, the averaged heat equation finally writes

$$\begin{aligned}\frac{\partial\bar T}{\partial t} + \boldsymbol{u}\nabla\bar T &= \frac{1}{c_p\bar\rho}\nabla(\overline{c_p\bar\rho\boldsymbol{u'}T'}) \\ &= \frac{1}{\bar\rho}\left[\nabla_h(A_H\nabla_h\bar T) + \frac{\partial}{\partial z}\left(A_V\frac{\partial\bar T}{\partial z}\right)\right] \qquad (2.38)\end{aligned}$$

The framework of this study allows some further simplification because of the geometric setup and the exclusion of higher order processes. Once again, the averaged heat equation in component notation for a discussion of the different terms:

$$c_p\bar\rho\cdot\left(\underbrace{\frac{\partial\bar T}{\partial t}}_{Local\,change} + \underbrace{\bar u\frac{\partial\bar T}{\partial x} + \bar v\frac{\partial\bar T}{\partial y} + \bar w\frac{\partial\bar T}{\partial z}}_{Advective\,terms}\right) = c_p\bar\rho\cdot\left(\underbrace{\frac{\partial}{\partial x}\overline{u'T'} + \frac{\partial}{\partial y}\overline{v'T'} + \frac{\partial}{\partial z}\overline{w'T'}}_{Turbulent\,terms}\right) \tag{2.39}$$

The first term on the left hand side of the equation vanishes since the overflow is assumed to be stationary, i. e. the properties of the overflow are time independent.

The coordinate system used in this study is oriented along the mean flow direction (see section 3.3 for further details). Therefore $\overline{u}$ is necessarily zero which eliminates the first advective term. The two remaining advective terms may be compared to each other as follows. A vertical mean velocity $\overline{w}$ may arise from a divergent Ekman transport at the bottom. The magnitude of $\overline{w}$ can be estimated from the mean downstream velocity $\overline{v}$ as it determines the Ekman transport T_E,

$$T_E = \frac{c_D \overline{v}^2}{f}, \tag{2.40}$$

with the bottom drag coefficient $c_D \sim 10^{-3}$ (KÄSE ET AL., 2003) and the Coriolis parameter f. Division of T_E by the Ekman layer depth d_E yields an estimate of the mean Ekman velocity $\overline{u_E}$. The Ekman velocity has its maximum at the plume core where the highest mean velocities $\overline{v}$ are reached. It decreases to the sides of the overflow plume. By making the assumption of zero Ekman velocity outside the plume $u_E(edge) = 0$, the divergence can be estimated:

$$\frac{\partial u_E}{\partial x} = \frac{u_E(core) - u_E(edge)}{x(core) - x(edge)} \tag{2.41}$$

This divergence must be balanced by a vertical velocity $\overline{w}$. It can be calculated from the equation of continuity:

$$\frac{\partial w}{\partial z} + \frac{\partial u}{\partial x} = 0 \Rightarrow w = \frac{\Delta u}{\Delta x} \Delta z \tag{2.42}$$

A mean downstream velocity $\overline{v} = 0.2\,\mathrm{m/s}$ leads to a mean Ekman velocity of $\overline{u_E} = 0.02\,\mathrm{m/s}$. The resulting vertical velocity is $\overline{w} = 4 \cdot 10^{-5}\,\mathrm{m/s}$. Estimating the temperature gradients to $dT/dz = 5 \cdot 10^{-3}\,\mathrm{{}^\circ K/m}$ and $dT/dy = 2 \cdot 10^{-6}\,\mathrm{{}^\circ K/m}$, the magnitude of the two remaining advective terms is

$$\overline{w} \frac{\partial T}{\partial z} = 2 \cdot 10^{-7} \qquad \overline{v} \frac{\partial T}{\partial y} = 1 \cdot 10^{-6}. \tag{2.43}$$

Hence, the horizontal advective term is approximately one order of magnitude larger than the vertical advective term[11]. The vertical advective term is neglected.

The two horizontal turbulent terms can be compared to each other. The divergence of turbulent motion in x–direction is very strong. There is a transition from (nearly) zero turbulent motion outside the plume to vigorous turbulent motion in the plume on a distance of less than 50 km. A chain of eddies travels with the overflow plume in y–direction, leading to only little changes in turbulent motion along the y–direction. The term with v' can thus be neglected.

---

[11] The estimate calculated here provides the upper limit of the vertical velocity. An opposite Ekman transport at the upper interface and non-zero Ekman transports at the plume edges lead to a reduction of the estimate.

The remaining terms represent an equilibrium between advection of temperature change on one side and turbulent heat exchange in x- and z-direction on the other side:

$$c_p \bar{\rho} \bar{v} \frac{\partial \bar{T}}{\partial y} = c_p \overline{\rho} \cdot \left(\frac{\partial}{\partial x} \overline{u'T'} + \frac{\partial}{\partial z} \overline{w'T'} \right) + \epsilon \tag{2.44}$$

Possible contributions of neglected terms are added as an ϵ.

This equation is of big importance in this study as with the available data it is possible to calculate two out of the three terms. Temperature measurements at different distances from the sill provide information about the advective term on the left hand side. The timeseries from moored current meters allow to calculate the horizontal turbulent heat flux (first term on the right hand side).

2.3.3 Past studies on entrainment

As shown in Fig. 1.2, Smith (1975) observes a decrease in average density contrast between plume and ambient water both in hydrographic data and in a streamtube model. The density contrast drops from $0.4 \cdot 10^{-3}$ g/cm^3 at the sill to $0.1 \cdot 10^{-3}$ g/cm^3 at 750 km downstream of the sill. Smith (1975) estimates the transport to increase from 1.3 Sv at the sill to 4.6 Sv some 900 km downstream. In the streamtube model, the strength of entrainment is parameterised by an empirical proportionality constant. An increasing entrainment constant leads to a faster decrease in density contrast, reduced downslope migration of the plume and increase in cross-sectional area of the plume. The bottom stress parameter is found to have less influence on the above-mentioned properties. In the streamtube model, the entrainment is linearly dependent of the plume velocity. Possible entrainment influencing factors like bottom topography, plume instability and vortex formation can not be accounted for in the one-dimensional model.

Dickson and Brown (1994) find an increase in transport from 2.9 Sv at the Denmark Strait sill to 5.2 Sv at a downstream distance of ~300 km. At the Angmagssalik mooring array at a downstream distance of 520 km[12], the transport has increased to 10.7 Sv. This increase is not only due to entrainment. The overflow waters from the Iceland-Scotland Ridge circulate through the Irminger Sea and join the DSOW. As the Iceland-Scotland Overflow Water (ISOW) is less dense, it settles above the DSOW. Nevertheless, the density range for that transports were calculated in the Angmagssalik array included the ISOW. At the southern tip of Greenland the transport has finally increased to 13.3 Sv.

In hydrographic observations Rudels et al. (1999) found a low salinity cap on top of the overflow plume which survived the initial descent of the overflow plume and became weak as the plume reached deeper than 2000 m. The capping indicates weak vertical mixing processes at the interface. The entrainment rate in the first part of the downstream way was found to be small. Rudels et al. (1999)

---

[12] The distance is defined to the mooring array of Macrander (2004) at the sill.

conclude that the initial waters within the plume merge close to the sill while the vertical entrainment there is not as strong as assumed before.

SMITH (1975) introduced an entrainment velocity w_e in his streamtube model. This velocity measures the flux of a property across the plume boundary. GIRTON AND SANFORD (2003) and KÄSE ET AL. (2003) estimate entrainment velocities from observations and a numerical model. GIRTON AND SANFORD (2003) find entrainment velocities of $4 \cdot 10^{-5}$ and $4 \cdot 10^{-4}$ $^{m}/_{s}$ before and after 125 km downstream of the sill, respectively. They also find that the overflow plume encounters steeper topography at this sill distance. Nevertheless, the specific process that drives the entrainment was not determined in their study. A numerical model by KÄSE ET AL. (2003) leads to an entrainment velocity of $5 \cdot 10^{-4}$ $^{m}/_{s}$

The results of past studies on entrainment in the DSO are summarised in table 2.3.3.

Table 2.2: *Past studies on entrainment into the Denmark Strait Overflow plume.*

	Transport increase (Sv)	Entrainment velocity (m/s)	Location (km downstream)	Warming rate
Smith (1975)	From 1.3 at the sill to 4.6 at 900 km downstream.			
Price and Baringer (1994)	From 2.6 at the sill to 4.1 at 100 km downstream.		Starts at 50, completed at 100.	1.5 °C on the first 100 km.
Dickson and Brown (1994)	2.9 at the sill, 5.2 at TTO and Dohrn, 10.7 at Angmagssalik, 13.3 at Cape Farewell		Close to the sill.	
Rudels et al. (1999)			Further away from the sill than suggested in earlier studies.	
Girton and Sanford (2003)	Similar to Dickson and Brown (1994).	$4\cdot10^{-5}$ before 125 km downstream, $8\cdot10^{-4}$ thereafter.	Increase at 125.	
Käse et al. (2003)	Similar to Dickson and Brown (1994).	$5\cdot10^{-4}$	Model: 100 Observations: Further downstream.	

3 Instruments and data processing

Observing currents in the ocean is a challenging task. Measurements at depths of several kilometers require robust instruments that resist high pressure and stay in position in vigorous ocean currents. The deployment and recovery of instruments in areas with heavy weather conditions such as the Irminger Sea is complicated and can be dangerous. Loss of instruments is unavoidable sometimes.

Successful collected data does not immediately provide the desired information. Oceanic motion consists of a multitude of physical processes on different timescales. A recorded ocean signal u is the sum of signals on different timescales:

$$u = \overline{u} + u_l + u_m + u_s \tag{3.1}$$

Here $\overline{u}$ is the mean of the signal, u_l stands for processes on long timescales, u_m denotes processes on transient timescales, as for example the eddies in the Denmark Strait Overflow, and u_s are the processes on short timescales inlcuding tides and inertial motions. In order to study one specific process, others have to be determined and filtered out.

This chapter gives an introduction into deep sea measurement methods, basic data analysis methods and filtering with application to the present survey with the main focus on transient time scales.

3.1 Current meter instruments

Mechanical current meters A mechanical current meter is shown in Fig. 3.1. It consists of a recording unit and a vane. The vane rotates the instrument into the direction of the current. The recording unit is equipped with a propeller that measures the speed of the current. Sensors for temperature, conductivity of the water and pressure can be attached to the recording unit. The recording unit has to be very tight to resist the pressure in more than 2000 m depth. Inside the recording unit is a compass. The direction of the current can be determinded from the orientation of the vane relative to the compass. All data is recorded to a watertight digital data storage unit.

The instruments have an accuracy of ± 1 $^{\mathrm{cm}}/_{\mathrm{s}}$ in speed, $\pm 5^\circ$ in direction and $\pm 0.05^\circ$C in temperature measurements. Most data in this study was recorded with mechanical current meters.

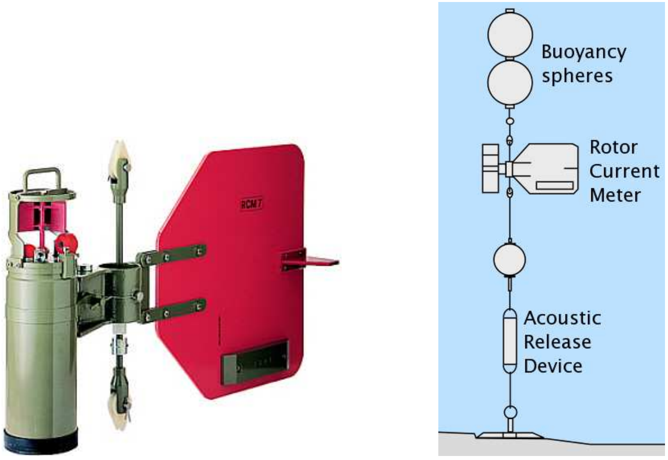

Figure 3.1: *Aandera current meter RCM8 (left) and the scheme of a mooring design (right). Both figures are from the current meter manufacturers homepage* `http://www.aanderaa.com`.

Acoustic current meters Modern current meters use an acoustic method to measure speed and direction of the current[1]. They use a sound signal that is backscattered by particles in the water. An acoustic pulse is emitted and the frequency shift of any incoming reflection is measured. By measuring in four directions, the Doppler effect in the sound signal gives information on the speed and the direction of the current. The acoustic method does not need any mechanical parts attached to the meter, thus they are insensitive to fouling.

Mooring design The meters are attached to a kevlar rope. Buoyancy spheres at the top of the mooring and above each instrument keep the mooring in an upright position. Sufficient buoyancy is very important, a tilt of the mooring line would lower the instruments. Such events may occur occasionally and can be seen in the data. The mooring is fixed to the seafloor with a heavy weight. An acoustic release device connects the kevlar rope to the anchor. For the recovery of the mooring, an acoustic signal is sent from the ship and prompts the releaser to disconnect the rope from the anchor. With the buoyancy spheres the mooring then ascends to the surface.

CTD measurements Measurements with conductivity-temperature-depth sensors (CTD) are a common mean for data collection in experimental oceanography. The conductivity is a measure for the salinity of seawater. In most cases, a CTD is attached to a water sampling device that is lowered from a ship. Vertical profiles of temperature, salinity and depth with a vertical resolution of a few cm can be obtained. Usually the data is averaged to 1 m bins.

---

[1] The acoustic current meters used at the *Institut für Meereskunde Hamburg* are manufactured by *RD Instruments* (`http://www.rdinstruments.com/`).

3.2 The mooring arrays

On the Greenland shelf slope off Angmagssalik[2] current measurements were made from 1986 to 1989 and again from 1995 until now. The instruments were deployed in several moorings at nominally the same locations for one year at a time. Fig. 3.2 shows the bathymetry of the area as well as the Angmagssalik array mooring positions from the deployment period 2001/2002. Also shown are the Dohrn[3] and TTO[4] mooring arrays. These two arrays were only deployed in 1990. The TTO array was deployed for a whole year, while the Dohrn array measured only for approximately 100 days.

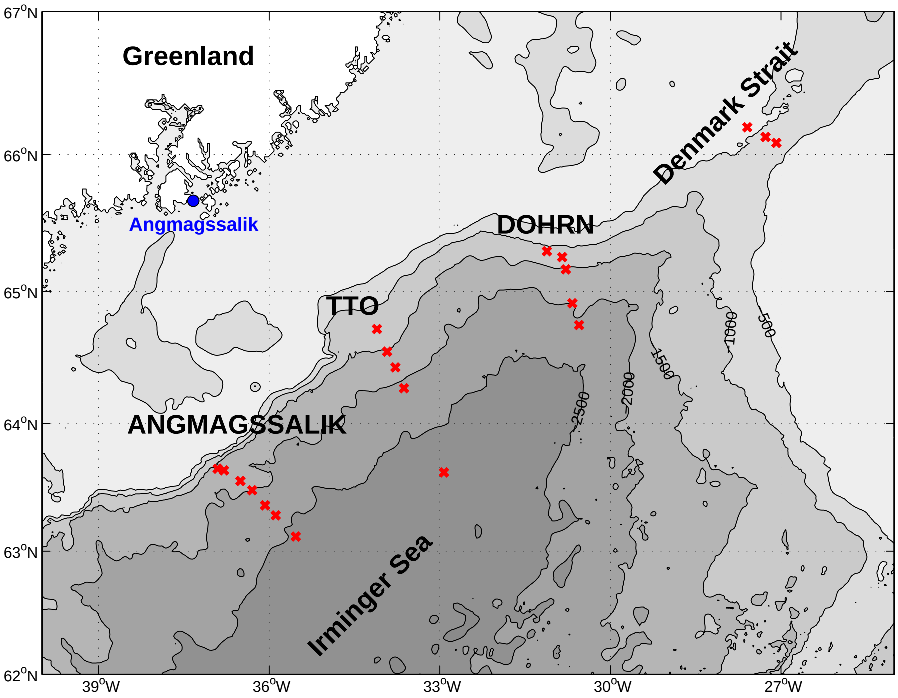

Figure 3.2: *Map of the mooring arrays south of the Denmark Strait. The positions of moorings at the sill, deployed by* MACRANDER *(2004), are shown additionally. The TTO and Dohrn array were only deployed in 1990. The Angmagssalik array was run from 1986 to 1989 and again from 1995 until now. The number of moorings in the Angmagssalik array varied from only two up to seven for each year. The positions of the Angmagssalik moorings shown here are from the deployment period 2001/2002. The names of the moorings, the number of instruments per mooring and their vertical distribution are given in Fig. 4.1 and Fig. 5.1.*

The position of the Angmagssalik array was chosen to measure the flux of North Atlantic Deep Water deriving from the overflows over the Greenland-Scotland Ridge.

---

[2] Angmagssalik was the old name for the town Tasiilaq on the Greenland coast.

[3] Named after the Dohrn Bank, a bathymetric feature on the Greenland shelf.

[4] Named after the expedition *Transient Tracers in the Ocean.*

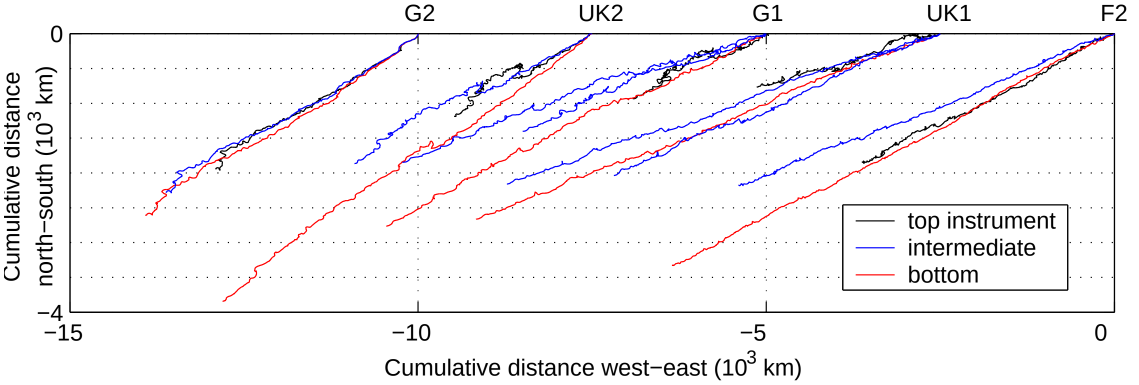

Figure 3.3: *Progressive vector diagrams of five moorings in the Angmagssalik array 2001. The axes have lengths as units as each velocity vector is multiplied with the sampling time of one hour.*

Here the overflow waters from east of Iceland have already reached the Greenland shelf slope after circulating around the Reykjanes Ridge and through the northern Irminger Sea. The upstream mooring arrays, TTO and Dohrn, were used together with the moorings at the Denmark Strait sill to estimate the overflow through Denmark Strait and the amount of entrainment from the sill to the arrays.

Most of the instruments in the mooring arrays were set up to measure current velocity and direction, temperature and pressure for determination of the instrument depth. In some cases sensors for salinity measurements were attached. The collected data was pre-processed by the CEFAS Lowestoft Laboratory including quality checks, despiking and interpolation of gaps in the timeseries.

Macrander (2004) deployed instruments directly at the sill. The positions of his moorings are shown additionally in Fig. 3.2. Temperature time series from these moorings will be used in chapter 6.

3.3 Axes rotation to mean flow direction

The current meter data is provided in the conventional coordinate system where U and V refer to the east and north components of the current. Fig. 3.3 shows a progressive vector diagram of the currents in the Angmagssalik array in this coordinate system. A preferred flow direction is apparent at all measurement points. They are all directed to the south-west. In detail, however, the mean flow direction varies slightly in between the moorings. It is appropriate to choose a coordinate system that is aligned with the mean flow direction for this steady current. Then the current data consists of along-stream and cross-stream components.

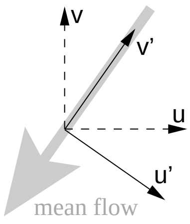

Figure 3.4: *New coordinate system.*

The overflow plume flows along the continental slope and follows the local bottom topography (Dickson and Brown, 1994). In the area of the Greenland shelf slope, the sea floor is furrowed by canyons. This leads to varying mean flow directions among the moorings (compare Fig. 3.3). Hence, not all moorings can be assigned the same direction. The coordinate system is allowed to vary among them.

The current time series are used to determine the direction of the mean flow by calculating the mean velocities $\overline{U}$ and $\overline{V}$. They form a vector that gives the angle of rotation α for the new coordinate system. A mean flow direction is computed for each mooring from the currents at intermediate height above bottom. The intermediate instruments are not affected by the bottom boundary layer and a possible Ekman transport[5]. Nevertheless, they are still deep enough to observe the overflow plume sufficiently. Therefore they are convenient for the computation of α.

The new components u and v are computed as

$$u = U \cdot cos(\alpha) - V \cdot sin(\alpha) \tag{3.2}$$

$$v = U \cdot sin(\alpha) + V \cdot cos(\alpha) \tag{3.3}$$

The components u and v are directed roughly towards northeast and southeast as drafted in Fig. 3.4.

3.4 Spectral analysis

The power spectral density (PSD) is computed to determine the dominant timescale in the variability of the current signal. The PSD gives the contribution of each frequency to the signal. In order to get a statistically reliable result, the spectrum is smoothed with a Hanning window. While this means loss in spectral resolution, an increase in degrees of freedom and hence a smaller confidence interval is the advantage of smoothing.

Fig. 3.5 exemplarily shows the PSD of the current velocity u at the bottom instrument of mooring G1. The high frequency range is dominated by two peaks, the M2 tide at 12.4 h and the inertial frequency around 13.4 h (see section 3.6). In this example, the highest variability is around a period of 7 days. This is in accordance with Dickson and Brown (1994) who estimate a dominant timescale of 3 to 12 days for the deep flow at the Angmagssalik mooring array.

3.5 Tides and high frequency motion

The high frequency domain u_s is governed by the tides and internal waves with the inertial period.

---

[5] The bottom stress leads to a deflection to the left of the current in the bottom boundary layer. The resulting transport of watermasses is called Ekman transport.

A well known part of the oceanic motion are the tides. Their deterministic behaviour allows to identify and remove the tidal part of a current signal. Any tidal signal is composed of a finite sum of sinusoids, the so called tidal constituents. Each of them has a specified frequency f_q and is either one of the principal constituents arising directly from planetary motion or a linear combination of these. With a number of M constituents the timeseries $x(t_n)$ can be written as

$$x(t_n) = \overline{x} + \sum_{q=1}^{M} \left[A_q \cos(2\pi f_q t_n) + B_q \sin(2\pi f_q t_n)\right] + x_r(t_n) \tag{3.4}$$

in which $\overline{x}$ is the mean of the record, $x_r(t_n)$ is the residual timeseries and A_q and B_q are the coefficients that determine amplitude and phase of each tidal constituent. In the least-squares analysis the variance of the residual timeseries, e.g. the squared difference of timeseries and the fit to the timeseries, is minimised. This results in $2M + 1$ simultaneous equations for the coefficients that can be solved as a matrix equation.

The number of possible constituents for the analysis is restrained by the Rayleigh criterion. This criterion is a measure for the required separation of neighbouring frequencies at a given record length. More precisely, the difference between two

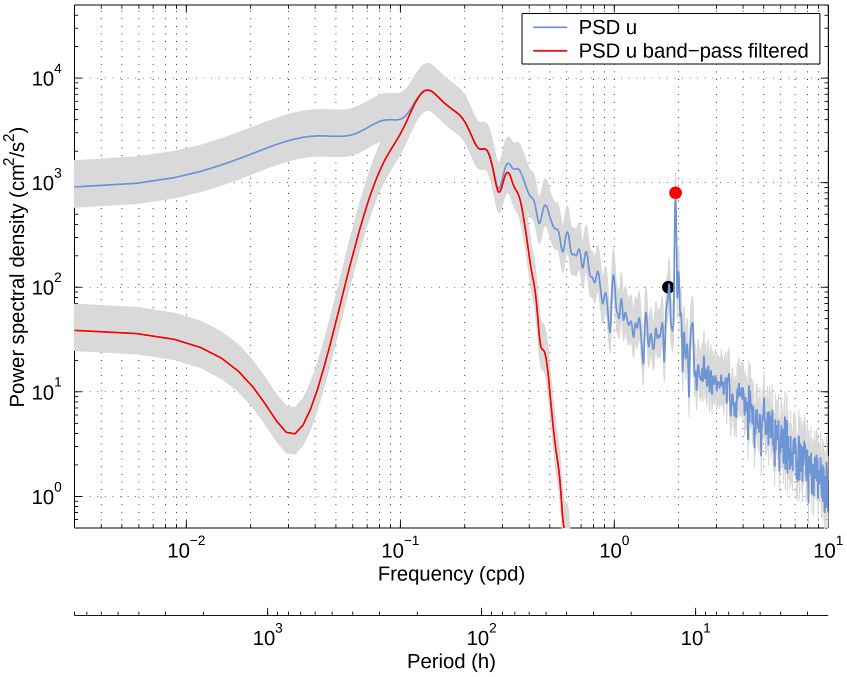

Figure 3.5: *Power spectral density of current velocity perpendicular to mean flow direction at mooring G1, 20 m above bottom (blue line). A Hanning window is used for smoothing. The 95 % confidence intervals are shaded grey. Inertial period and M2 tide are marked with a black and red dot, respectively. Also shown is the bandpass filtered timeseries (red line). See section 3.6 for a description of the bandpass filter.*

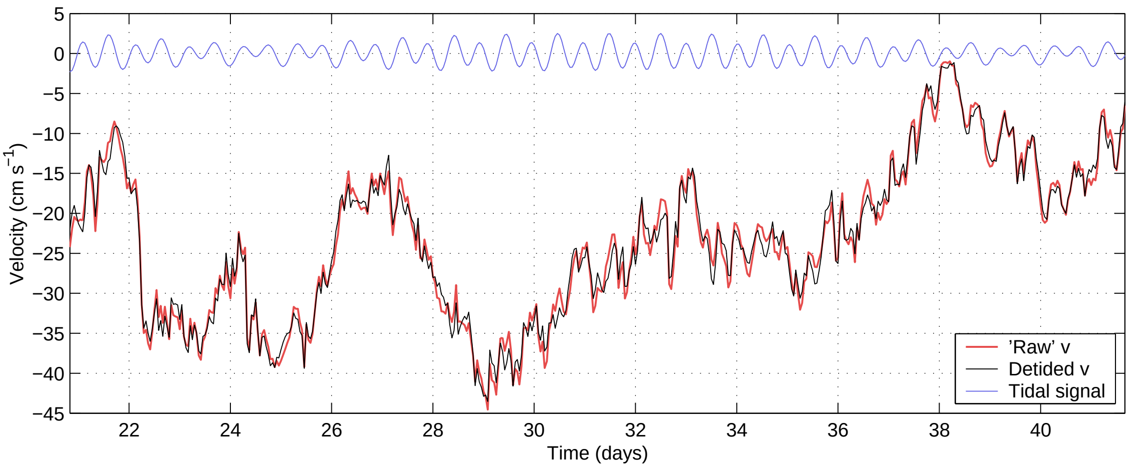

Figure 3.6: *Current velocity in mean flow direction (red) and tidal signal (blue) for the bottom instrument at mooring G1. The detided time series is shown in black.*

neighbouring frequencies times the record length should be bigger than one. For the timeseries with a length of almost one year approximately 60 constituents can be included in the analysis. To exclude constituents with a high uncertainty, the signal to noise ratio (SNR) of all constituents is calculated. In a second computation, only those constituents with $SNR > 1$ are used.

The tidal analysis was performed with the Matlab toolbox `t_tide` provided by Pawlowicz et al. (2002). This software fits the tidal constituents to the data with the least squares harmonic analysis method. The residual timeseries are calculated for further analyses by substraction of the tidal signal, an example is shown in Fig. 3.6. Only a small fraction of the variability in the time series arises from the tides.

Since the tides are removed already, internal waves with frequencies close to the inertial frequency will be important for the design of a bandpass filter. The inertial frequency is given by

$$\omega = \frac{2\pi}{f} \tag{3.5}$$

with the Coriolis parameter f. For 63° north, the inertial period is 13.4 h. This means that a bandpass filter with a cut-off period of about one day already filters out variability with the inertial period.

3.6 Bandpass filter

Meso-scale motions with timescales of 3–10 days are of interest in this study. This corresponds to the processes on transient timescales u_m in equation 3.1. They can be extracted from the signal with a bandpass filter. The expression bandpass refers to the frequency domain that is not blocked by the filter while constituents of the

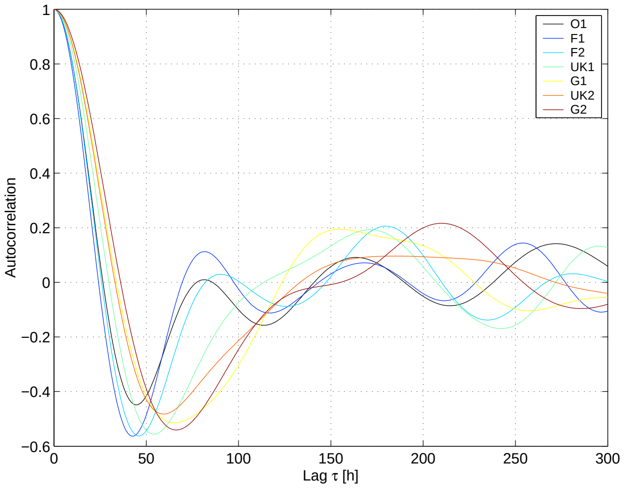

Figure 3.7: *Autocorrelation functions of bandpass filtered bottom current velocities u.*

signal with frequencies outside this domain are removed from the timeseries.

The autocorrelation functions of the bandpass-filtered bottom velocities u are shown in Fig. 3.7. The autocorrelation function is one by definition, when the time lag is zero. The first maximum is at a time lag that corresponds to the dominant time-scale in the time series. Here the dominant timescale increases as greater depths are reached. This also the case for the component in mean flow direction (not shown in the figure). All spectra of the time series in the Angmagssalik mooring array peak on time-scales between 3 and 10 days. This is consistent with the observed surface eddies.

The careful analysis of the power density spectra in the preceding section and the dominant physical processes provide sufficient information for a reasonable time-frame. Nevertheless, the choice of filter parameters that determine the frequency range of the passband is somewhat arbitrary.

In the low frequency domain u_l, seasonal, annual and inter-annual variability are to be excluded. The overflow is stable on large timescales as no seasonal fluctuations are observed (Dickson and Brown, 1994). Only inter-annual variability might occur (Fig. 3.8). This means that the choice of parameter is not very important in the low frequency end. The high frequency domain was already discussed in section 3.5.

A 3$^{\text{rd}}$ order Butterworth filter with cut-off frequencies of $^1/_{60\,\text{h}}$ and $^1/_{300\,\text{h}}$ is chosen. This includes the variability range of 3–10 days that was in found in section 3.4. While for a perfect filter the cut-off frequencies would mark the step from 0 to 1 magnitude and vice versa in the frequency response, for the real filter that is used it denotes the frequencies that have $\sqrt{1/2}$ magnitude. Fig. 3.9 shows the frequency response of the used filter. The order of the filter determines the slope of the transition between stop-band and pass-band. A higher order leads to a steeper

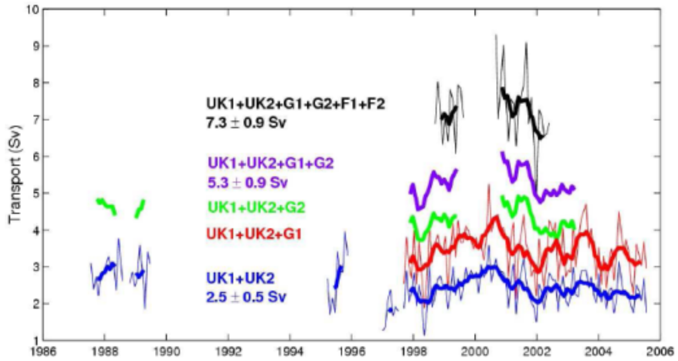

Figure 3.8: *Transports in the Angmagssalik array (*ASOF-W, *2006). The transport timeseries suggest that the overflow is variable on interannual timescales. This interannual variability was also observed at the DS sill by* Macrander et al. *(2005). No seasonal signal is observed.*

transition but generates overshoot ripples, known as Gibbs' phenonemon (Emery and Thomson, 1998). Leakage of energy into the filtered record is the result. The overshoot ripples can already be seen in the 4th and 5th order Butterworth filters also shown in Fig. 3.9.

Fig. 3.10 compares filtered current velocity and temperature with the unfiltered data. The meso-scale variability can be extracted from the original time series.

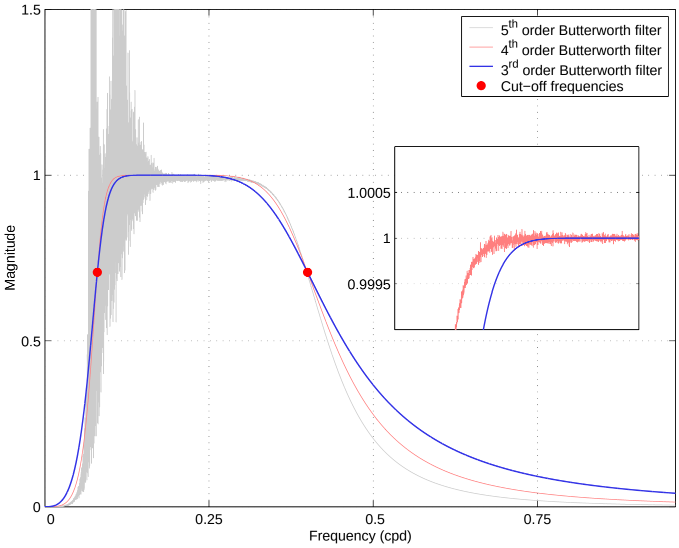

Figure 3.9: *Frequency response of a 3rd order Butterworth filter (blue line). A 4th and 5th order Butterworth filter is shown in red and grey to exemplify Gibbs' phenonemon. The cut-off at periods of 60 and 300 h is marked with red dots. The inset shows the better transition of the 3rd order filter at the high frequency end of the passband.*

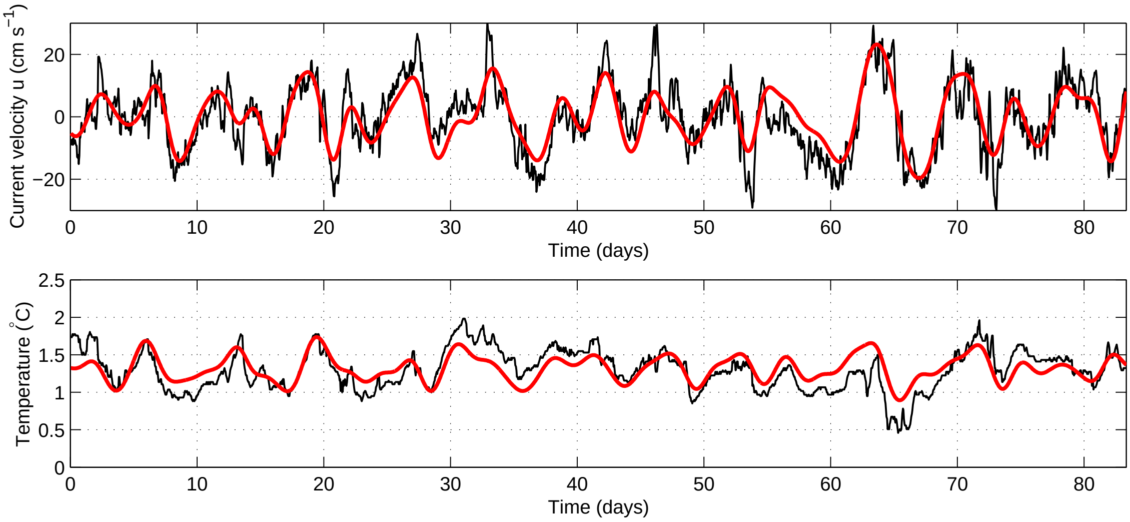

Figure 3.10: *Bandpass filtered time series of current velocity u' and temperature T' (red) and the unfiltered timeseries u and T (black). The mean temperature $\overline{T}$ was added to the filtered temperature T' to make it comparable to the original timeseries. The mean velocity $\overline{u}$ was substracted from the unfiltered velocity timeseries for the same reason.*

4 Eddy mixing in the Angmagssalik array

Some characteristic features of the overflow plume in the Angmagssalik mooring array are presented in this chapter. The heatfluxes that are driven by the eddies presented in section 2.2 are calculated and, with the assumption of this being a stationary process, the warming of the plume through eddy-induced mixing is estimated.

4.1 Characteristics of the overflow plume

The structure of the overflow plume in the Angmagssalik array can be shown by averaging current velocity, temperature and energies over a whole deployment period, i. e over one year. This method gives a characteristic picture of the plume. It is done with the dataset from the Angmagssalik array between July 2001 and June 2002. This dataset offers both good spatial and temporal coverage of the plume and has little instrument failure.

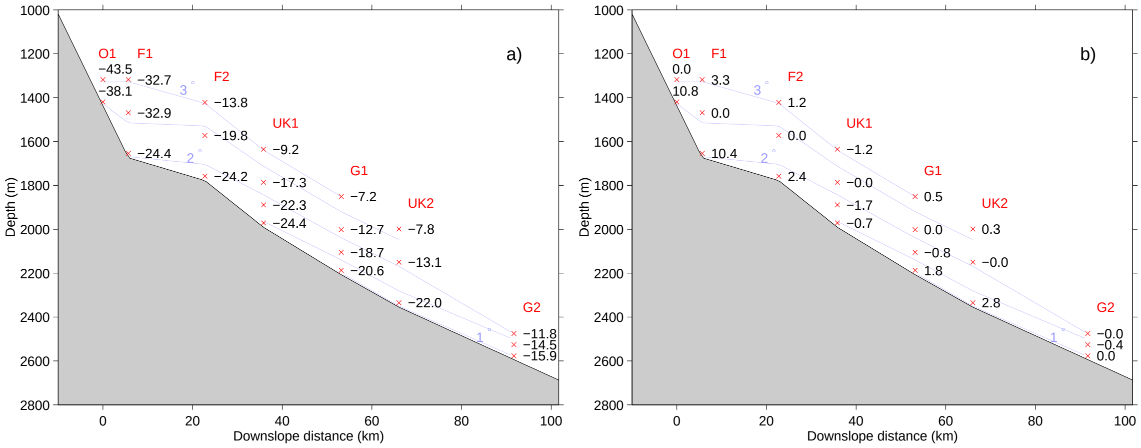

Figure 4.1: *Cross section of mean current velocities $\overline{v}$ and $\overline{u}$ ($^{cm}/_{s}$) along (a) and perpendicular (b) to mean flow direction, respectively. Positive values point towards northeast (v) and southeast (u). Red crosses show the positions of the current meter instruments, red labels the mooring code. Isotherms calculated from mean temperatures are shown in blue.*

Mean velocities A cross-section of the mean velocity in the mean flow direction ($\overline{v}$) is shown in Fig. 4.1a. Isotherms that are calculated from the mean temperatures are plotted in addition. The overflow plume may be identified as water colder than 2.5 °C. This matches approximately the potential density definition of $\sigma_\theta \geq 27.80$ by DICKSON AND BROWN (1994). The highest mean velocities in the overflow plume are found close to the bottom. The mean velocities decrease with increasing height above bottom. The mean velocities decrease downslope at moorings UK2 and G2. Very high mean velocities are observed at the upslope moorings O1 and F1.

The intensification of the flow at the bottom reflects the baroclinic nature of the overflow plume as reported by KÄSE ET AL. (2003) for the region downstream of the Denmark Strait sill. The downslope decrease of the mean velocity indicates the edge of the plume. However, mooring G2 measures mean velocities above 10 $^{\mathrm{cm}}/_{\mathrm{s}}$, thus the mooring array does not seem to cover the complete width of the plume. It is ambiguous how the high mean velocities upslope are reached. They are found in water not dense enough to account for the DSOW. The high velocities could be due to the steeper bottom topography.

The mean velocities perpendicular to the mean flow direction ($\overline{u}$) are shown in a cross section in Fig. 4.1b. They are very small compared to the velocities in mean flow direction. The values at the instruments that were used to calculate the direction of the mean flow are of course zero by definition. Most of the mean speeds at the bottom are directed downslope. This indicates the effect of bottom friction and a resulting Ekman current. The small values of $\overline{u}$ justify the use of only one coordinate system per mooring, i. e. one mean flow direction for all instruments of a mooring.

Mean kinetic energy The mean kinetic energy K_M of the flow can be calculated from the mean velocities:

$$K_M = \frac{1}{2}(\overline{u}^2 + \overline{v}^2). \tag{4.1}$$

A cross section of the mean kinetic energies is shown in Fig. 4.2a. Large mean kinetic energies are observed close to the bottom. The mean kinetic energy decreases with downslope distance. DICKSON AND BROWN (1994) found that the mean kinetic energy in the overlying watermasses is close to zero. The highest values are at the upslope moorings outside of the DSOW. All this reflects the distribution of the mean velocities in mean flow direction as is evident from the calculation of K_M.

Mean eddy kinetic energy With the bandpass filtered velocity timeseries a mean eddy kinetic energy K_E can be calculated:

$$K_E = \frac{1}{2}(\overline{u'^2} + \overline{v'^2}) \tag{4.2}$$

It gives the kinetic energy of the fluctuations within the frequency range that was chosen for the bandpass filter. A cross-section of the mean eddy kinetic energy is

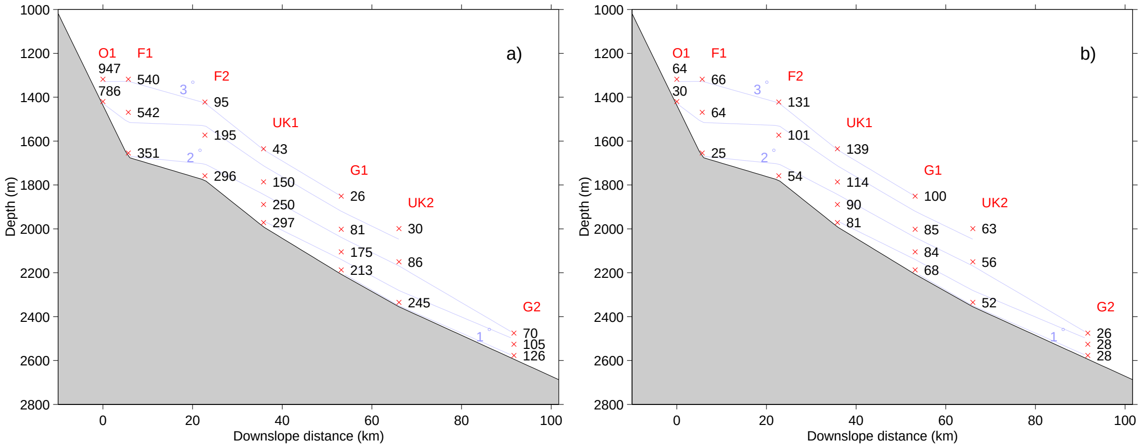

Figure 4.2: *Cross section of mean kinetic energy K_M (a) and mean eddy kinetic energy K_E (b) per unit mass (cm^2/s^2).*

shown in Fig. 4.2b. The highest mean eddy kinetic energies are observed in the centre of the array around mooring UK1. It decreases at the edge of the plume. In contrast to the mean kinetic energies, the mean eddy kinetic energy increases with height above bottom. This is in accordance with Krauss (1996), he found the maximum speed in an eddy on top of the DSOW.

Variability in plume height A mean height of the overflow plume was estimated from the isotherms in the cross-sections. Fig. 4.3a shows the temperature fluctuations $\overline{T'^2}$. The largest fluctuations are observed close to the upper plume boundary. This suggests that the height of the overflow plume is variable itself. Fig. 4.3b shows the temperature variations with depth and time at mooring UK1. Domes of cold water are passing the mooring. This compares to the cold domes closer to the sill observed by Girton and Sanford (2003).

The plume height variability has approximately the same frequency as the current velocities. The tank experiments described in section 2.2.4 suggested a connection between eddies and the thickness of the dense water layer. Fig. 2.9 shows the dense domes in a tank experiment.

It is not only the temperature fluctuations but also the increasing eddy kinetic energy with height above bottom (Fig. 4.2b) that reflects the variability in plume thickness. As the upper instruments are situated close to the plume boundary, they may be temporarily outside the plume and thus measure low speeds. This contributes to the high variability.

The plume characteristics presented in this section were calculated with the 2001/2002 dataset. The calculations were also done with datasets from other deployment periods. The mean values varied for the other deployment periods. The mean kinetic energy for example varied by approximately 30%. This compares with the long-term changes in plume transport (Macrander et al., 2005). Nevertheless, the

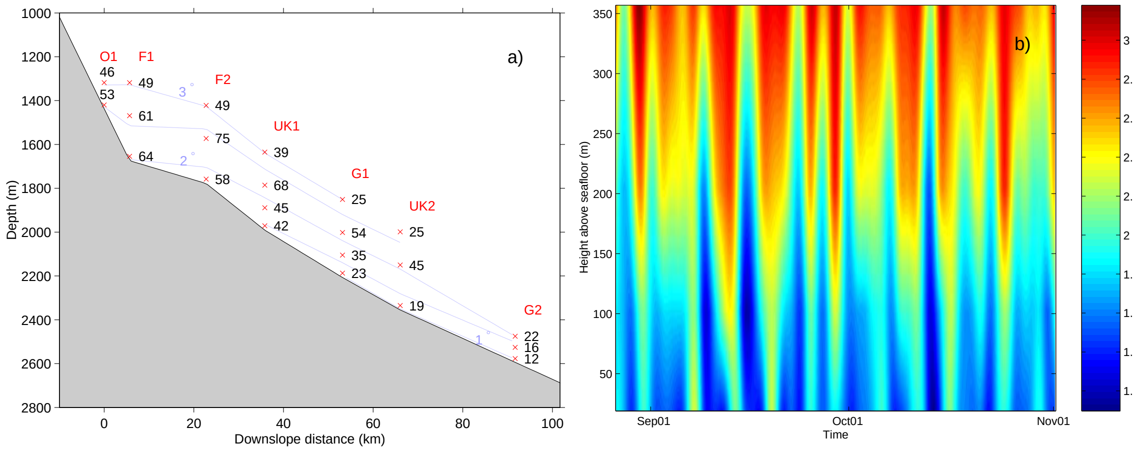

Figure 4.3: *Cross section of Temperature fluctuation* $\overline{T'^2}$ *(*$K^2 \cdot 10^3$*) (a), temperature variations with depth and time at mooring UK1 (colourscale in* $^\circ C$*) (b).*

structure of the plume remained the same over all the deployment years.

4.2 Eddy heat transport

The data from the 2001/2002 mooring array is used to calculate eddy driven heat fluxes into the overflow plume.

The plume momentum in u-direction was found to be highly variable on timescales between 3 and 9 days (section 3.4). The stick plot in Fig. 4.4 shows that this variability is not just a meandering current. In several cases, the current direction changes in a rotational sense.

In Fig. 1.2 it was shown that the entrainment of ambient water into the overflow plume leads to a decrease of the plume density. The density of seawater is a function of temperature, salinity and pressure. For the overflow region, the density is dominated by the temperature. This can be seen in CTD profiles of the Angmagssalik array where both temperature and salinity decrease with depth while density increases. Hence, a transport of heat into the overflow plume must be the driving mechanism for the change in plume density.

Rotational motion does not lead to a net water mass transport since

$$\overline{u'} = 0. \tag{4.3}$$

A net heat flux can be accomplished, though, by the transport of warm and cold water in opposite directions:

$$\overline{u'T'} \neq 0 \tag{4.4}$$

It is therefore the product of bandpass filtered velocity perpendicular to the mean flow direction and temperature ($\overline{u'T'}$) that provides an estimate of the role of hori-

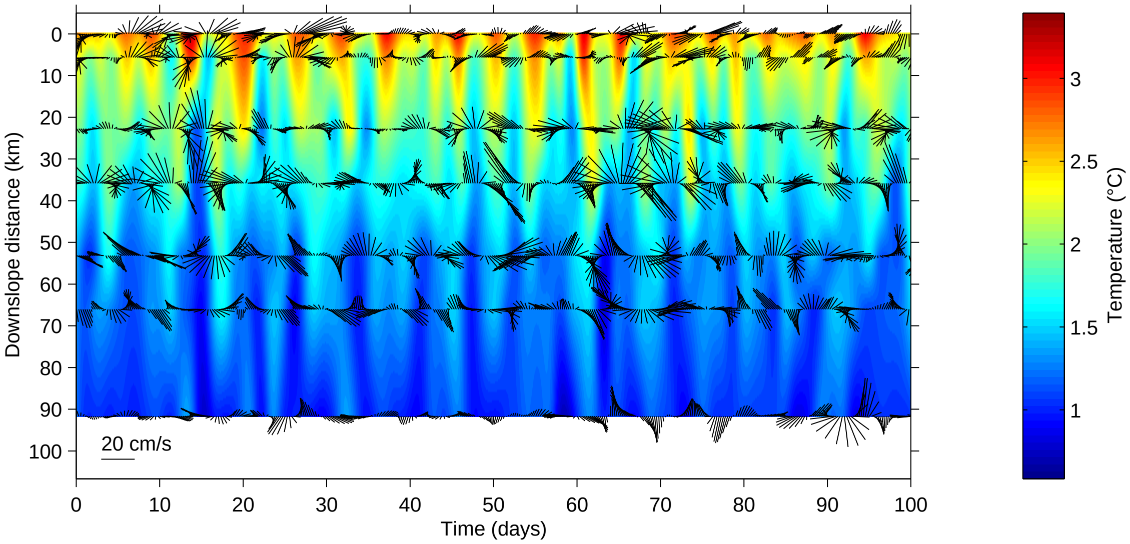

Figure 4.4: *Bandpass filtered current meter data (black sticks) together with temperature (coloured) of the bottom instruments. A scale for for the vectors is given to the lower left.*

zontal motion with mesoscale variability in the mixing process. This corresponds to the first term on the right hand side of the averaged heat equation (2.44).

The mean eddy heat fluxes $\overline{u'T'}$ in the Angmagssalik array are shown in Fig. 4.5. The region with the highest eddy kinetic energy around mooring UK1 (see Fig. 4.2) also is the region of highest $\overline{u'T'}$. However, there is no simple linear relationship between eddy kinetic energy and eddy heat flux. At the moorings F1 and UK2 the eddy kinetic energies are almost as high as at UK1, but the eddy heat fluxes are one order of magnitude less. The direction of $\overline{u'T'}$ has a similar pattern for all moorings. The eddy heat flux is directed downslope at the bottom. The direction reverses with increasing height above seabed. In both cases, the heat flux is opposite to the temperature gradient. Thus, heat is transported from warm into cold regions.

Referring to the main question whether the mesoscale variability leads to a mixing of overflow plume and ambient water, it can be stated that net eddy heat fluxes occur for the single measuring points. However, it is not clear if this results in a net warming of the overflow plume since the direction of these fluxes reverses on a vertical distance of only one hundred meters.

For the further calculation of a possible warming-up of the plume, its lateral boundaries have to be determined. The overflow plume is defined by its density and, since the density in the overflow is dominated by temperature, an isotherm can be used to set a plume boundary. The choice of the limiting isotherm is somewhat arbitrary. The 2.5°C isotherm is chosen here, but calculations will also be done for the 2.0°C and 3.0°C isotherms for comparison.

The isotherm as the upper plume boundary and the mooring lines, acting as 'side walls', divide the plume into several 'boxes'. These boxes are 2-dimensional. For

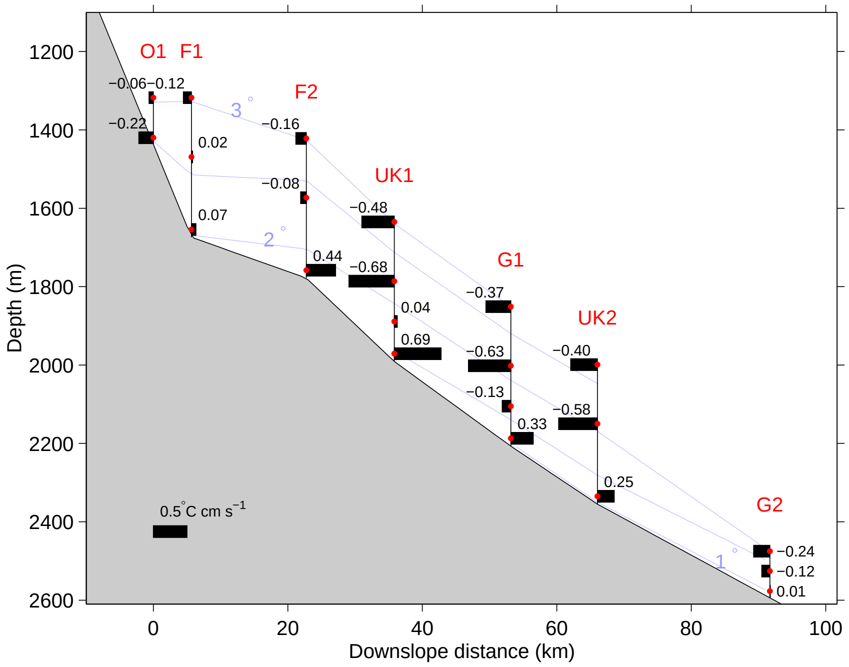

Figure 4.5: *Cross section of mean eddy heat fluxes* $\overline{u'T'}$ *(°Ccm/s). The black bars give direction and amount of mean eddy heat transport (also labelled with numbers). A scale for the black bars is given to the lower left. Positive values correspond to a transport to the right. Isotherms are shown as blue lines.*

the calculation of their volume, their length is taken be 1 m. The box volume V_{box} is

$$V_{box} = \Delta x \cdot \frac{\Delta z_1 + \Delta z_2}{2} \cdot 1\text{m} \tag{4.5}$$

where Δx is the distance between two moorings and Δz_i is the height above bottom of the plume boundary on each side of the box. For these boxes, a net heat transport is calculated by vertical interpolation and subsequent vertical integration of the heat fluxes.

4.2.1 Interpolation methods

There are usually three or four data points on each mooring line over a vertical distance of 300 m. Two different methods are used for an interpolation of these points. In the first method, the profiles are interpolated linearly between the instruments and taken constant elsewhere. The second method uses polynomials for data inter- and extrapolation.

Fig. 4.6a shows the result of the two interpolation methods for the temperature profiles. The height of the 2.5°C isotherm differs only slightly between the two methods, except for moorings O1 and G2 where only data points close to the bottom are available. For these, the polynomial method is more appropriate as suggested

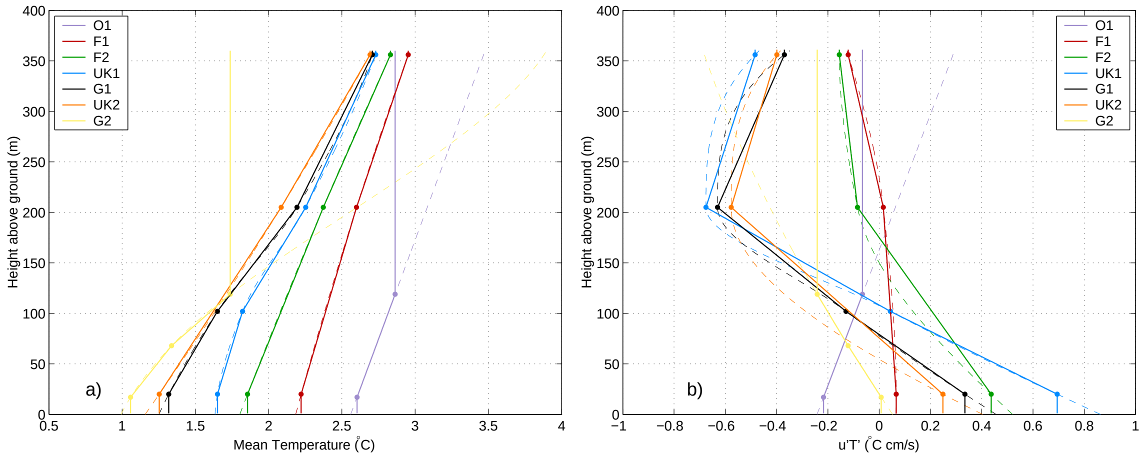

Figure 4.6: *Vertical interpolation of* $\overline{T}$ *(a) and* $\overline{u'T'}$ *(b). Solid lines show linear interpolation, dashed lines result from polynomial interpolation. Annual mean values* $\overline{u'T'}$ *and* $\overline{T}$ *used for the interpolation are drawn as dots.*

by the other temperature profiles. Since O1 is outside the 2.5°C range, only the temperature interpolation at G2 is used. The upper plume boundary is determined with the results of the polynomial interpolation.

The vertical interpolation of the eddy heat transport is more complicated as it changes direction with increasing height above bottom. The same two interpolation methods as described for the temperature profiles are used, but in this case they result in a larger difference (see Fig. 4.6b). Again, only values below the 2.5°C isotherm are used to calculate the warming-up of each box, respectively. Hence, the error of the strong difference at G2 is only small, O1 is not even used. The polynomial method probably overestimates the downslope transport for the moorings in the centre of the array.

The following calculations will be done for both interpolation methods to provide an error estimate.

Information about the bottom boundary layer (BBL) can not be extracted from the data and effects arising from bottom friction are neglected. This may be justified with the small thickness of the BBL compared to the integration intervals between bottom and upper plume boundary.

4.2.2 Net eddy heat transport into the plume

A transport with velocity $\boldsymbol{v}$ of a property ψ through a surface $\boldsymbol{A}$ is

$$\psi\rho\boldsymbol{v}\cdot\boldsymbol{A}. \tag{4.6}$$

The eddy heat transport Q_{eddy} per time interval into the boxes defined by the moorings and the upper boundary can be calculated with the extrapolated values $\overline{(u'T')_H}$.

The sideface A of the boxes is the height above bottom of the plume boundary H_{box} times the unit length of 1 m. The eddy heat transport at each mooring reads

$$\frac{\Delta Q_{eddy}}{\Delta t} = c_p\,\rho \sum_{H=0}^{H_{box}} \overline{(u'\,T')_H} \cdot 1\text{m}. \tag{4.7}$$

In this calculation, the density ρ is set constant to 1027.9 $^{\text{kg}}/_{\text{m}^3}$ and the specific heat capacity of seawater c_p is 4187 $^{\text{J}}/_{\text{kg K}}$.

The eddy heat transports resulting from the polynomial interpolation method and the 2.5°C upper plume boundary are shown in Fig. 4.7. The convergences of the eddy heat transports give the net eddy heat transport into each box. A net warming is found between the moorings F2 and UK2. This is the region of the plume core (Fig. 4.2). The highest convergence in eddy heat transport is between F2 and UK1. The water at the plume edges is cooled by the eddy heat transport.

The results for all three plume boundary definitions and the two interpolation methods are listed in table 4.1. The warming of the three plumes differs in the position of the convergent region of eddy heat transport within the plume. This region is situated downslope for the 2.0°C-plume[1] while it is more pronounced upslope for the 3.0°C-plume.

The temperature change of the water in a box with volume V_{box} (eq. 4.5) with the mass $M_{box} = \rho V_{box}$, resulting from a heat input ΔQ, is

$$\Delta T = \frac{\Delta Q}{c_p M_{box}}. \tag{4.8}$$

The warming rate for each box, i. e. the temperature change per unit time, can be calculated from the net eddy heat transports into the boxes. Replacing ΔQ in equation 4.7 with equations 4.8 and 4.5 yields

$$\frac{\Delta T}{\Delta t} = \frac{\sum_{H=1}^{H_b} \overline{u'\,T'}_H \cdot 1\text{m}}{V_{box}}. \tag{4.9}$$

It may be assumed that the process of eddy heat transport into the plume core is not only happening in the Angmagssalik array, for which the calculations were carried out here, but over a longer alongstream distance $\Delta\,\xi$ where the eddies are observed. By making the assumption that this eddy heat transport is regionally a steady process, a warming rate per downstream distance can be calculated. The time period for which the plume is exposed to the eddy mixing process can be calculated from the mean plume velocity. The eddy driven warming rate along the plume pathway ξ is

$$\frac{\Delta T}{\Delta \xi} = \frac{\Delta T}{\Delta t} \cdot \frac{1}{\overline{v}}. \tag{4.10}$$

---

[1] In the following discussion, the term 2.0°C-plume denotes the overflow plume defined by the 2.0°C isotherm.

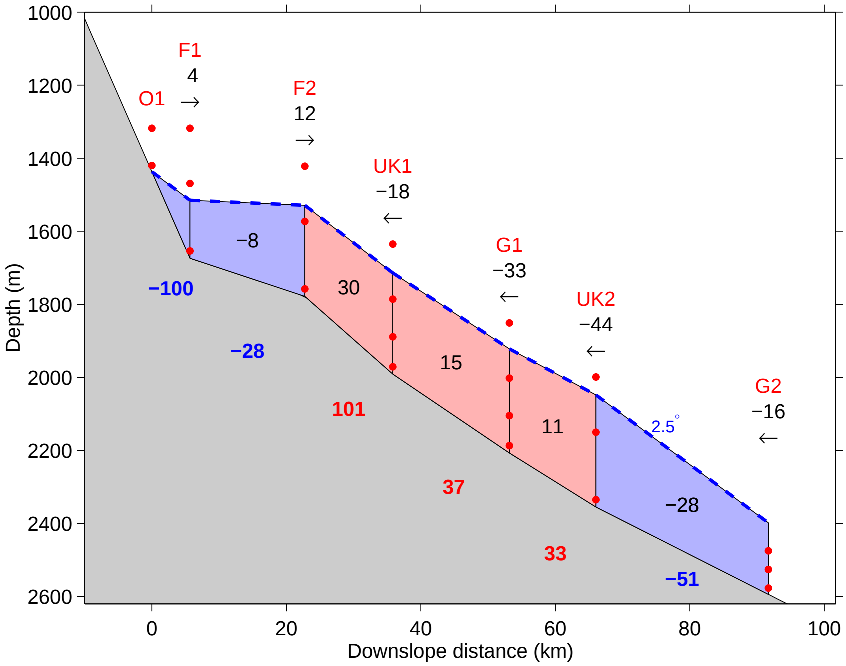

Figure 4.7: *Net eddy heat transport* $\Delta Q/\Delta t$ *(*$10^5\,\mathrm{J/m\,s}$*) through the mooring lines up to the 2.5°C isotherm. Values from the polynomial interpolation method for* $\overline{u'T'}$ *are used in the calculation. Arrows mark the direction of the eddy heat transport. The convergences (red boxes) and divergences (blue boxes) of the net eddy heat transport are printed into each box. Red and blue values below the boxes give the eddy driven warming rate* ΔT *per 100 km in mK for each box. The red dots show the position of the instruments.*

A mean velocity of 20 cm/s is estimated for the Angmagssalik array from the cross section of the mean velocities in mean flow direction (Fig. 4.1a). This is less than the mean bottom velocity of about 25 cm/s as it should give a vertical averaged value.

For later comparison with plume warming rates derived from direct temperature measurements along ξ, the plume warming rate along a distance of 100 km is calculated. The results for the two interpolation methods and the three plume boundary definitions (2, 2.5 and 3°C) are shown in table 4.1. The results of the polynomial interpolation are discussed below before a comparison of the two interpolation methods leads to an error estimate of the warming rates.

The eddy driven warming rate for the 2.5°C-plume reaches its highest value between the moorings F2 and UK1. A warming rate of ~0.1 K per 100 km is calculated there. The warming rate for the whole convergent region, i. e. the plume between moorings F2 and UK2, is 54 mK per 100 km. The warming rates derived from the two other plume boundary definitions are of the same order. The convergent regions gain 72 mK in the 2.0°C-plume and 45 mK in the 3.0°C-plume.

The two interpolation methods provide a mean for an error estimate. Table 4.2 compares the warming rates of the convergent plume regions for both interpolation methods. The warming rates of the 2.5°C-plume and 3.0°C-plume differ only by

Table 4.1: *Eddy heat fluxes* $\Delta Q/\Delta t$ *(*10^5 *J/s) and the resulting warming rates* ΔT *per 100 km (mK) for a mean plume velocity of 20 cm/s in the Angmagssalik array. The results are given for the three different plume boundary definitions and the two interpolation methods linear (L) and polynomial (P).*

Limit	Interpolation	O1–F1		F1–F2		F2–UK1		UK1–G1		G1–UK2		UK2–G2	
		$\Delta Q/\Delta t$	ΔT	$\Delta Q/\Delta t$	ΔT	$\Delta Q/\Delta t$	ΔT	$\Delta Q/\Delta t$	ΔT	$\Delta Q/\Delta t$	ΔT	$\Delta Q/\Delta t$	ΔT
2.0°C	L	0	0	-12	-223	-4	-35	18	77	5	25	2	4
	P	0	0	-12	-218	-5	-39	19	80	12	63	-6	-17
2.5°C	L	-3	-88	-12	-42	31	103	15	36	4	12	-21	-37
	P	-4	-100	-8	-28	30	101	15	37	11	33	-28	-51
3.0°C	L	-9	-72	-9	-18	44	107	10	18	0	0	-25	-38
	P	-10	-76	-4	-8	44	109	10	19	6	14	-30	-45

Table 4.2: *Plume warming rate per 100 km of the part of the plume that has a convergence in eddy heat transport. This is the region between F2 and UK2 for the 2.5°C-plume and 3.0°C-plume and the region between UK1 and UK2/G2 for the 2.0°C-plume.*

Boundary	Linear	Polynomial	Difference
2.0°C	31 mK	72 mK	43 %
2.5°C	48 mK	54 mK	11 %
3.0°C	40 mK	45 mK	11 %

11 % between the two methods. The 2.0°C-plume has a difference of 43 %. This is mainly due to the inclusion of the UK2–G2 region in the linear interpolation method. It has very low values. If they were negative and thus the UK2–G2 region was excluded, the error would be only 25 %. Nevertheless, the difference between the two interpolation methods is less than 50 % for all results. This even holds for most of the single boxes as can be seen in table 4.1.

4.3 Summary and discussion

From the timeseries in the Angmagssalik mooring array it was found that

1. The overflow plume is highly variable on time scales between 3 to 9 days.
2. The variability is not just a meandering current, but dominated by rotational motion.
3. Horizontal eddy heat transports perpendicular to the mean flow ($\overline{u'T'}$), obtained from bandpass filtered timeseries with cut-off periods 60 h and 300 h, are highest in the region of the plume core.
4. The eddy heat transports lead to a warming of the plume core between moorings F2 and UK1. This warming is accompanied with a cooling of the plume edges.
5. It is assumed that the eddy heat transport that was found in the Angmagssalik array is a regionally steady process. With a mean plume velocity of 20 $^{\text{cm}}/_{\text{s}}$, the warming rate per 100 km reaches values as high as 0.1 K. The mean warming rate of the plume core is around 50 mK.
6. The region of convergent eddy heat transport shifts downslope with decreasing height of the plume boundary definition.
7. Errors resulting from the two different interpolation methods are below 50 % for the convergent regions. This even holds for most of the single boxes that were calculated.

The horizontal eddy heat flux is broadening the plume as the core is warmed and the edges are cooled. This means that the overall volume transport of the dense overflow plume increases. It is concluded that the eddies contribute to the entrainment into the overflow plume. However, the relative importance of the eddies in the entrainment process is not clear yet.

5 Eddy heat transports at the Dohrn and TTO arrays

The two mooring arrays Dohrn and TTO, situated 160 and 320 km upstream of the Angmagssalik array, are used to estimate eddy heat transports closer to the sill. As for the Angmagssalik array, the characteristics of the overflow plume at the two arrays are presented first before eddy heat fluxes are calculated.

5.1 Plume characteristics

The Dohrn and TTO mooring arrays are situated at distances of 200 and 360 km downstream of the DS sill (see Fig. 3.2 for the mooring locations). Both arrays were deployed in 1990. The TTO array was deployed for a whole year while the Dohrn array measured for approximately 100 days. Nevertheless, this shorter time period is still long enough to capture at least 20 eddies when the eddy period is below five days. This is the case in the Dohrn array as will be shown in this section. Hence, it provides statistics good enough to calculate eddy heat fluxes.

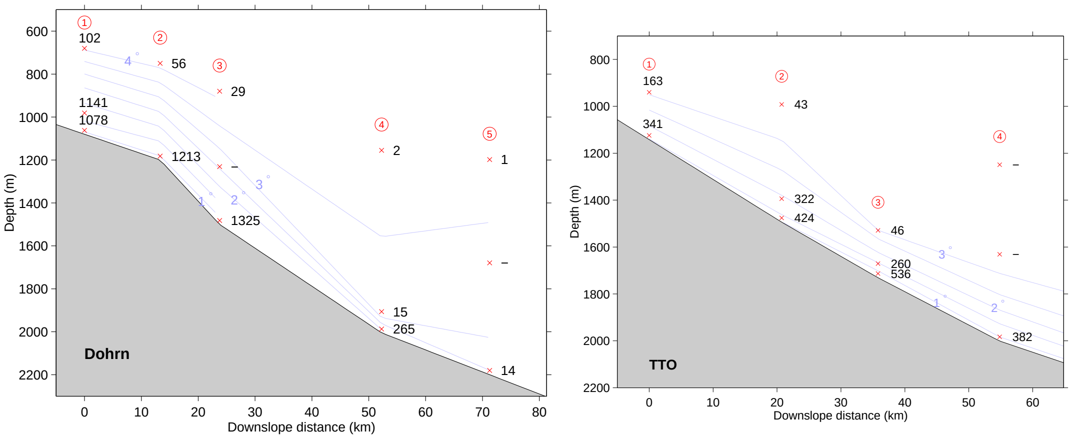

Figure 5.1: *Mean kinetic energy per unit mass (cm^2/s^2) in the Dohrn and TTO arrays. Some instruments were erroneous and provide no values, they are marked with a dash. Isotherms are shown as blue lines. One mooring in the TTO array at 160 km downslope distance was too far away to measure the overflow plume and is not shown here (see Fig. 3.2 for mooring positions).*

Mean kinetic energy Fig. 5.1 shows the mean kinetic energy at the two arrays. The isotherms derived from the mean temperatures are shown in addition. In the Dohrn array, closest to the sill, the lower isotherms are squeezed in downslope direction. This indicates that the plume is located up on the slope and has not reached greater depths yet. The plume core is in a depth of around 1500 m. At the TTO array it has descended to around 1800 m according to the distribution of the isotherms.

The Dohrn array has the highest kinetic energy at the bottom. The flow has a pronounced baroclinic structure as the mean kinetic energy decreases with height above bottom. The low mean kinetic energy at mooring number four indicates the lower edge of the plume. This is also suggested by the squeezed isotherms, showing a small plume height. Mooring number five is completely out of the overflow plume as the mean kinetic energy is close to zero. The mean bottom speeds are around 50 $^{\mathrm{cm}}/_{\mathrm{s}}$ (not shown).

The mean kinetic energy in the TTO array shows a baroclinic structure of the flow as well. The lower plume edge is not resolved as good as in the Dohrn array. However, a fifth mooring in the TTO array at 160 km downslope distance was completely outside the overflow plume and is not shown. The mean bottom speeds in the TTO array are around 30 $^{\mathrm{cm}}/_{\mathrm{s}}$.

Mean eddy kinetic energy The mean eddy kinetic energy increases with height above bottom in both the Dohrn and the TTO array. The magnitude of the mean eddy kinetic energy is highest around the plume core.

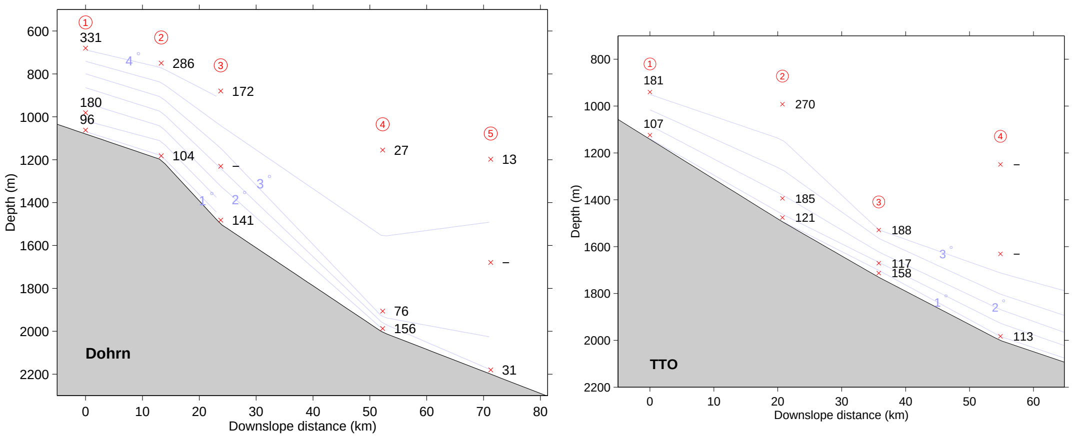

Figure 5.2: *Mean eddy kinetic energy in the Dohrn and TTO arrays. One mooring of the TTO array is not shown as explained in Fig. 5.1. Isotherms are shown as blue lines.*

In the Dohrn array, the highest mean eddy kinetic energy is located at the upper instrument of mooring one. This high value may be produced by the EGC measured by the upper instrument at times. The high bottom eddy kinetic energy at mooring four in the Dohrn array again indicates the lower edge of the overflow plume. A meandering plume would let the instrument measure the flow only at times, giving rise to the high eddy kinetic energy. The decreasing eddy kinetic energy with height above bottom and the smaller spacing between the lower isotherms at this mooring support this assumption.

Dominant timescales The spectral analysis is shown in Fig. 5.3. The dominant frequency is the highest in the Dohrn array with around 0.5 cycles per day. It decreases to approximately 0.25 cpd in the TTO array.

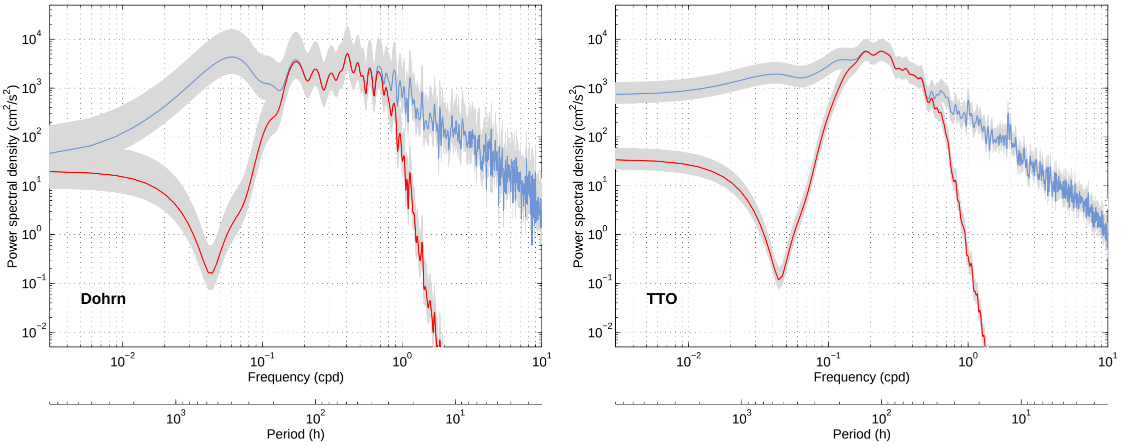

Figure 5.3: *Power spectral density of current velocity perpendicular to the mean flow direction (u) in the Dohrn array (mooring 3, bottom instrument) and the TTO array (mooring 2, bottom instrument). Blue lines show the PSD of the time series. The red lines show the bandpass filtered PSD. The 95 % confidence intervals are shaded grey. Notice that the shorter time series from the Dohrn array leads to larger confidence intervals.*

The PSD of the Dohrn array time series do not show a pronounced maximum as can be seen in the TTO spectra. The highest energy in the Dohrn array is around a period of 18 days. This period is too long to account for the meso-scale eddies. For the bandpass filter in the Dohrn array, cutoff periods of 28 and 200 h are chosen. The low frequency motions are excluded with this parameters. The tidal signal in the Dohrn array is very weak, the M2 partial tide is not observable in the Dohrn spectrum.

The cutoff periods for the bandpass filter for the TTO array are set to 36 and 200 h. In contrast to the Dohrn array, the M2 partial tide is strong here.

Comparison with the Angmagssalik array The mean kinetic energies at the Dohrn array are four times higher than at the Angmagssalik array and still two to three times higher than in the TTO array. This is of course consistent with the mean bottom speeds that are around 50 $^{\mathrm{cm}}/_{\mathrm{s}}$ in the Dohrn array and 25 $^{\mathrm{cm}}/_{\mathrm{s}}$ in the Angmagssalik array. The baroclinic structure of the flow is the same in all three arrays.

The distribution of the mean eddy kinetic energy across the plume has the same structure in the three arrays. It has its maximum at the core of the plume and increases with height above bottom. The magnitude of the mean eddy kinetic energy is approximately the same in the two upstream arrays. In the Angmagssalik array the eddy kinetic energy decreases to only half the value.

The dominant time scale increases from a period of around two days in the Dohrn array to approximately four days in the TTO array. In the Angmagssalik array the period is even longer with around seven days.

5.2 Eddy heat transport

The coordinate systems at each mooring in the two upstream arrays is rotated to the mean flow direction. The timeseries are detided and bandpass filtered as described for the Angmagssalik array in chapter 3. Solely the parameters for the bandpass filters are different as described in the preceding section.

The eddy heat fluxes in the two arrays are shown in Fig. 5.4. The eddy heat fluxes at the bottom converge in the centre of the plume at both arrays. This indicates that the whole plume core is covered by the mooring arrays. The magnitude of the eddy heat fluxes is approximately the same in both arrays. Solely the eddy heat flux at the bottom instrument of mooring four in the Dohrn array is five times larger than all other eddy heat fluxes calculated here. This is the point where the plume edge is situated in the preceding section. It appears to be a region of strong mixing, possibly because of the strongly inclined isotherms. Strong diapycnal mixing induced by horizontal eddy motion can take place here.

The eddy heat fluxes at the two arrays are approximately twice as high as at the Angmagssalik array.

The net eddy heat transports into boxes and the eddy driven warming rates are calculated as for the Angmagssalik array in chapter 4. The resulting net eddy heat transports into the plume, limited again by the 2.5°C isotherm, are shown in Fig. 5.5. The highest convergence in eddy heat transport is found at the upper part of the slope at both arrays. At the lower edge of the plume at the Dohrn array strong cooling is observed. This results from the high eddy heatflux in combination with the small volume of the box. The data from the TTO array was not sufficient for a calculation of the eddy heat transport at the lower part of the slope.

At both arrays the magnitude of the convergences in heat transports is approximately three times higher than at the Angmagssalik array. The highest value is found upslope in each array. However, lowering the upper plume boundary to 2°C does not shift the convergent region downslope here as it was at the Angmagssalik array. In the Dohrn array, the region of convergent eddy heat transport for the 2.0°C-plume is even shifted upslope as only the upper two boxes show a net warming.

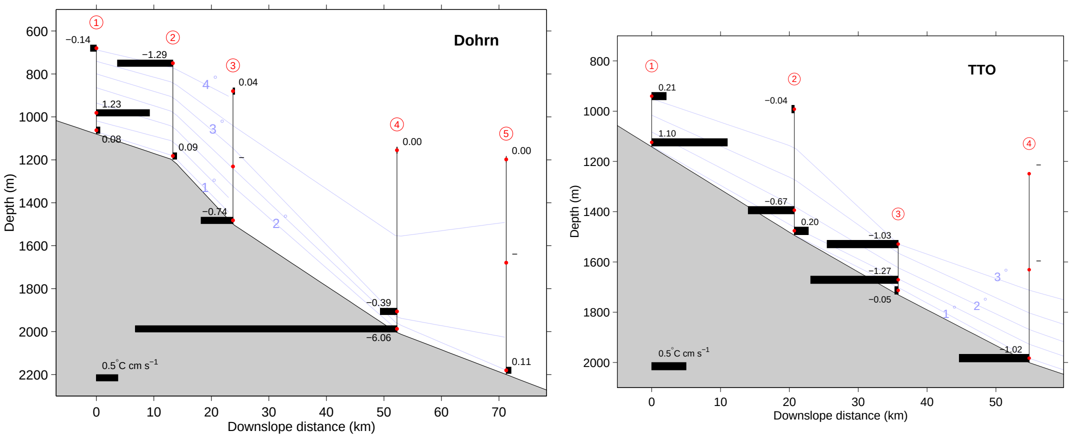

Figure 5.4: *Mean eddy heat fluxes* $\overline{u'T'}$ $(^{\circ}C\,{}^{cm}/_{s})$ *in the Dohrn and TTO arrays. Black bars give direction and magnitude of the mean eddy heat transport. A scale for the black bars is given to the lower left. Positive values correspond to a downslope transport. Isotherms are shown as blue lines.*

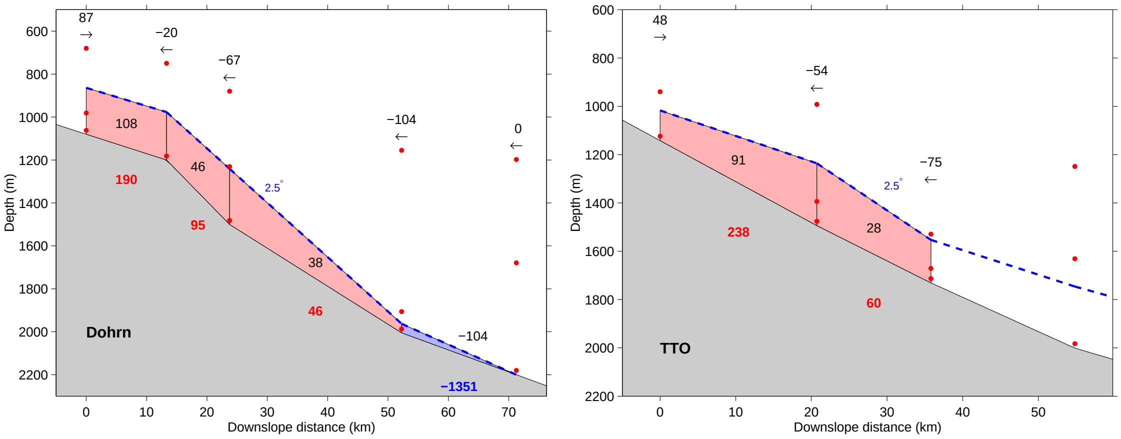

Figure 5.5: *Net eddy heat transport* ${}^{\Delta Q}/_{\Delta t}$ *(*$10^5\,{}^{J}/_{m\,s}$*) through the mooring lines up to the 2.5°C isotherm in the Dohrn and TTO arrays. Values from the polynomial interpolation method for* $\overline{u'T'}$ *are used in the calculation. Arrows mark the direction of the eddy heat transport. The convergences (red boxes) and divergences (blue boxes) of the net eddy heat transport are printed into each box. Red and blue values below the boxes give the eddy driven warming rate* ΔT *per 100 km (mK) for each box. The red dots show the position of the instruments.*

To calculate plume warming rates from the heat transports, the mean plume velocity has to be used to estimate the time that the eddy mixing process can act on the plume. Cross sections of $\overline{v}$ in the two arrays (not shown here) show a mean plume velocity of 45 ${}^{cm}/_{s}$ for the Dohrn array while at the TTO array the plume has slowed down to 25 ${}^{cm}/_{s}$. The values given here are slightly less than the mean bottom velocities in the previous section. They are chosen to represent the mean velocity up to the plume boundary. The baroclinic structure of the flow leads to a lower mean plume velocity when vertical averaging is applied. However, compared to the Angmagssalik array the plume velocities are still high. They lead to shorter time periods that the eddy mixing is effective than further downstream downstream.

The resulting plume warming rates per 100 km for the two arrays are printed below the boxes in Fig. 5.5. High eddy induced plume warming rates with around 0.2 $^{\mathrm{K}}/_{\mathrm{100km}}$ are reached at the upper part of the slope in both arrays. The overall warming rates per 100 km for the parts of the plume that have a convergent eddy heat transport are given in table 5.1. They are about 120 $^{\mathrm{mK}}/_{\mathrm{100km}}$ in the Dohrn array and about 160 $^{\mathrm{mK}}/_{\mathrm{100km}}$ in the TTO array. While the eddy heat transports are approximately the same in the two arrays (see Fig. 5.2), the smaller mean plume velocity in the TTO array leads to the higher eddy induced warming rates.

The two interpolation methods differ by 10 % in the Dohrn array and only 3 % in the TTO array. This is somewhat surprising as the spatial resolution is lower here than in the Angmagssalik array.

In the Angmagssalik array the eddy induced warming rates are around 50 mK. Hence, they are two to three times larger here. The TTO array has the highest warming rates.

Table 5.1: *Plume warming rate per 100 km in the Dohrn and the TTO array. The plume warming rate is calculated for the part of the plume that has a convergence in eddy heat transport.*

Boundary	Linear	Polynomial	Difference
Dohrn			
2.0°C	132 mK	138 mK	4 %
2.5°C	92 mK	102 mK	10 %
3.0°C	89 mK	99 mK	10 %
TTO			
2.0°C	179 mK	182 mK	2 %
2.5°C	153 mK	157 mK	3 %
3.0°C	144 mK	149 mK	3 %

5.3 Summary and discussion

For the two mooring arrays Dohrn and TTO it was found that:

1. Mean kinetic energy and mean eddy kinetic energy are higher than at the Angmagssalik array while their distribution across the plume is similar at all arrays.
2. The dominant time scale increases from a period of ∼2 days at the Dohrn array to ∼4 days at the TTO array and ∼7 days at the Angmagssalik array.
3. The mean eddy heat fluxes are about the same and two times higher than in the Angmagssalik array.
4. At a point in the Dohrn array with strongly inclined isotherms, the eddy heat flux is much higher than at all other instruments, indicating strong eddy induced mixing at the edge of the plume.
5. The eddy driven warming rates are higher than in the Angmagssalik array. They have a maximum in the TTO array.
6. The downward shift of the convergent region of eddy warming for a lower plume boundary could not be observed here. The opposite was rather observed.
7. The error resulting from the two interpolation methods is surprisingly small in the TTO array with only 3 % difference. It is also small in the Dohrn array with 10 % difference between the two methods.

The eddy driven warming rates found here support the conclusion that the eddies contribute to the entrainment into the overflow plume.

The increase in eddy driven plume warming rate from the Dohrn to the TTO array is a somewhat surprising result. In a numerical model with realistic bottom topography, KÄSE ET AL. (2003) found a spontaneous event of increased barotropic vorticity correlated with a baroclinic transport maximum at ∼ 240 km. They relate this eddy activity to baroclinic instability. For the distance of the Dohrn array (∼ 200 km), their Fig. 10 shows a minimum in barotropic vorticity which then is consistent with the little pronounced meso scale variability in the PSD of the Dohrn array found here.

6 Downstream warming of the overflow plume

The warming-up of the overflow plume on its way downstream is calculated from temperature measurements along the plume pathway ξ in this chapter. The plume warming along ξ corresponds to the left hand term of the averaged heat equation (eq. 2.44).

Two different kinds of data are available for the calculation of mean plume temperatures at different distances ξ. Time series from mooring arrays provide a high temporal resolution of the plume temperature. Hydrographic sections, run normal to the mean flow direction, provide a larger number of measuring points in the vertical, across and along the plume. Both data sets are used here to benefit from their advantages.

6.1 Temperature time series from mooring arrays

The downstream mooring arrays Dohrn, TTO and Angmagssalik, and the additional mooring array directly at the DS sill, provide temperature time series that allow to calculate mean plume temperatures at different locations along ξ. Fig. 3.2 gives the positions of the mooring arrays. All time series have a length of approximately one year except the Dohrn array that was only deployed for three months.

One way to find the temperature change along ξ is to compare the bottom temperatures of the plume. The bottom temperatures are less affected by the changing plume height than the upper ones as could be seen in the temperature variability in Fig. 4.3 a. To match the core of the plume, three time series from each array with the lowest mean temperatures are chosen.

The mean bottom temperatures from the four mooring arrays, together with their standard deviations, are shown in black in Fig. 6.1. To obtain only one mean temperature for each mooring array, the average of the three mean values mentioned above is calculated. The mean bottom plume temperature increases strongly on the first 200 km from the sill. Thereafter, only a small increase is observed. The variability of the plume leads to large errorbars.

In a review of *The Dense Northern Overflows*, SAUNDERS (2001) gives mean potential temperatures for the Dohrn, TTO and Angmagssalik array that are higher than the mean bottom temperatures found here. He does not provide information

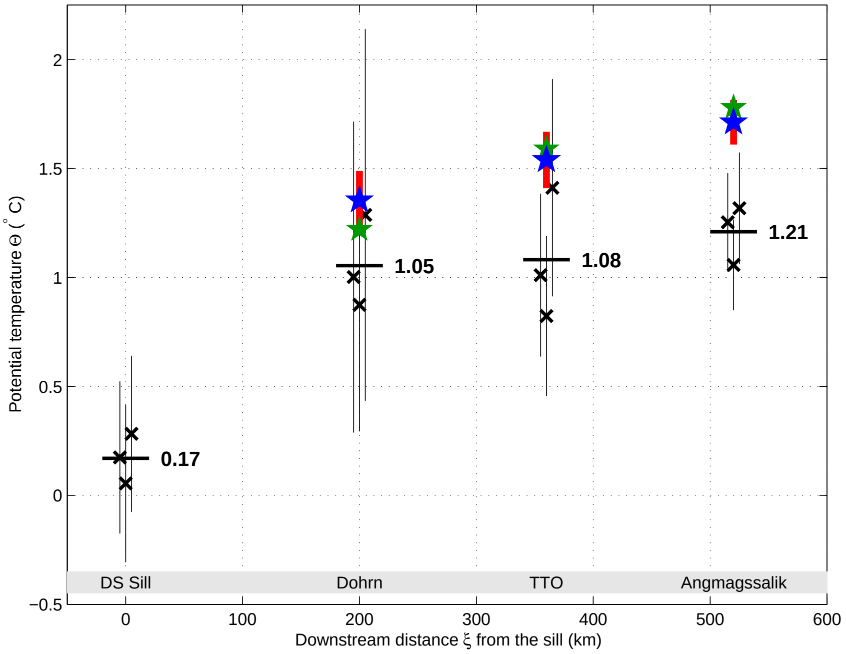

Figure 6.1: *Bottom temperatures from moored thermometers (20 m above bottom) at the DS sill, Dohrn, TTO and Angmagssalik array. The three lowest mean temperatures from each array were chosen to represent the plume core. They are marked with black crosses, the corresponding vertical black lines give the σ-confidence interval. Horizontal black lines give the mean of the three lowest mean temperatures per mooring array. The horizontal spacing between between the three values of each array was only introduced for better visibility. Green stars mark the mean plume temperatures reported by* Saunders *(2001), probably calculated by averaging over the whole plume. The vertical red lines give the range for plume temperatures calculated by vertical averaging over different numbers of instruments (see text). Blue stars give the mean of these.*

about his method of determination of a mean plume temperature, but the higher temperatures in his review suggest that some vertical averaging is used in his calculation of the mean plume temperatures. In this way, mean plume temperatures are calculated here by averaging over different numbers of instruments. The coldest mean values are chosen again to match the plume core, but some of the upper instruments are included. In the Angmagssalik four to six mean values are chosen. In the two upstream arrays the spatial coverage of the plume is smaller and only four to five instruments are useful for this estimation method. The instruments at the Denmark Strait sill were only located at the bottom, thus this calculation method cannot be applied there. The mean of the results from different numbers of instruments matches approximately with the values from Saunders (2001). They are shown as blue and green stars in Fig. 6.1.

6.2 Hydrographic sections along the plume pathway

Repeat hydrographic surveys have been carried out downstream of the Denmark Strait since 1997. Fig. 6.2 shows a composite of the position of all hydrographic stations from 1997 to 2005. The sections are called ASOF[1] I to VI. ASOF V was rarely occupied and thus not used in this study. The distance between the DS sill and ASOF I is approximately 200 km. The sections are equally spaced at a distance of 160 km (ASOF IV to ASOF VI is 320 km because of the missing ASOF V). The sections ASOF I, II and III coincide with the Dohrn, TTO and Angmagssalik mooring arrays.

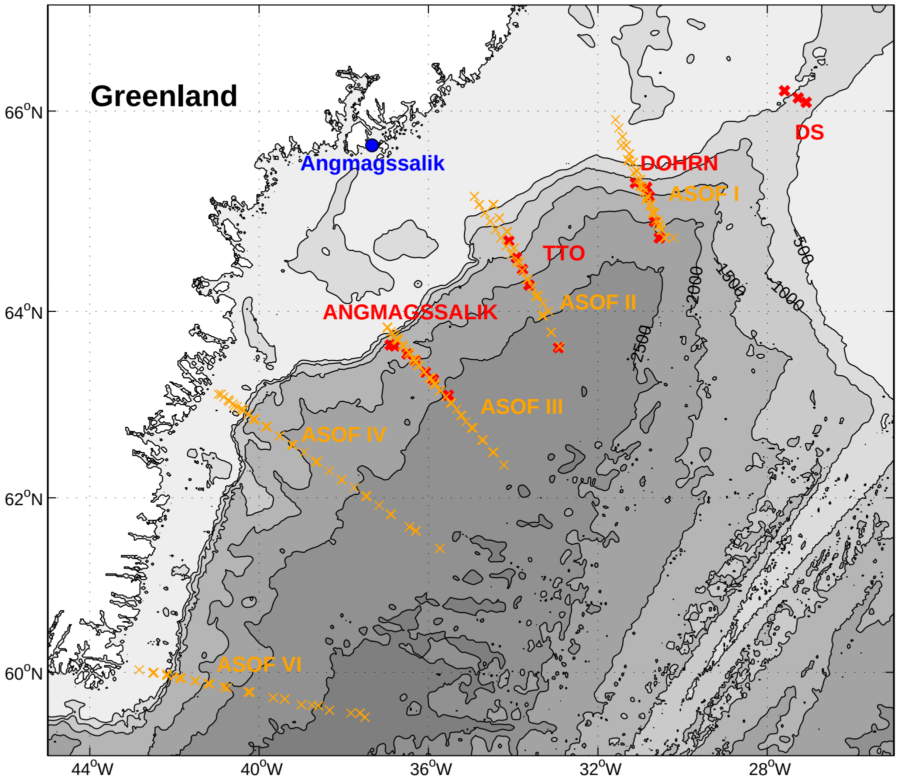

Figure 6.2: *Map of hydrographic sections south of the Denmark Strait (only the stations relevant for the overflow plume are shown here). The orange crosses show CTD stations of hydrographic surveys from 1997 to 2005. Lines ASOF I to ASOF IV were occupied each year, data is missing for line ASOF VI in the years 1998 and 2005. The positions of the moorings and the names of the mooring arrays are marked red.*

Temperature and density profiles from the occupation of all five sections in June and July 2001 are shown in Fig. 6.3. The overflow plume is characterised by low temperature and high density anomalies. The deepening of the overflow plume

---

[1] Named after the EU-funded project *Arctic/Subarctic Ocean Fluxes.*

becomes apparent from section I to VI as the anomalies are found at increasing depths. The strong gradients between the cold water of the overflow plume and the warmer ambient water are weakened on the way downstream.

For each section, a mean plume temperature may be defined as follows:

1. Calculate the bottom temperature for each profile by averaging over the lowest 50 m.
2. Take the profile with the lowest bottom temperature of each section and year. This should give the bottom temperature of the plume core.
3. Calculate one mean plume temperature for each section from the mean values of all years.

The resulting bottom plume temperatures for each year (step 2) and their mean value (step 3) are shown in Fig. 6.4. The mean temperature decreases from ASOF I to ASOF II. From thereon, the mean temperatures indicate a warming of the plume along the plume pathway to ASOF VI. The decrease in mean plume temperature between ASOF I and ASOF II is a surprising result. It can be explained with the meso-scale variability of the Denmark Strait overflow. The high meso-scale variability may lead to aliasing of the measured temperature fields. Section ASOF I may have been occupied at times with almost no overflow water present, while the section downstream covers the cold core of an overflow pulse. The consequence is a downstream plume cooling, contrary to what is observed in the mooring temperature timeseries in the preceding section. The pulsating character of the overflow plume was shown for the Angmagssalik array in Fig. 4.3 b, and is even more pronounced closer to the sill. There the overflow can cease completely for periods of a few days (KÄSE AND OSCHLIES, 2000). Hence, the number of CTD datasets is not sufficient for reliable statistics.

All dots of one colour in Fig. 6.4 belong to the same year. The high variability can be seen by looking at values of a specific year. In the 1997 survey (brown dots), no overflow water colder than 2°C was measured in section I. The temperature drops from 2.06°C to 0.75°C from section I to section II. This must be due to the overflow pulses mentioned above. As the plume travels along the shelf, the pulses are smoothed by mixing processes. The high variability in the region of ASOF I is also indicated by the errorbars of the mean temperatures in the Dohrn array (Fig. 6.1). They are the largest of all four mooring arrays. I conclude that the temperature decrease from ASOF I to ASOF II in mean and median values is not a real trend but merely due to the low temporal resolution of the hydrographic data. This is supported by the mean temperatures from the mooring time series where no decrease in the mean plume temperature was found (Fig. 6.1).

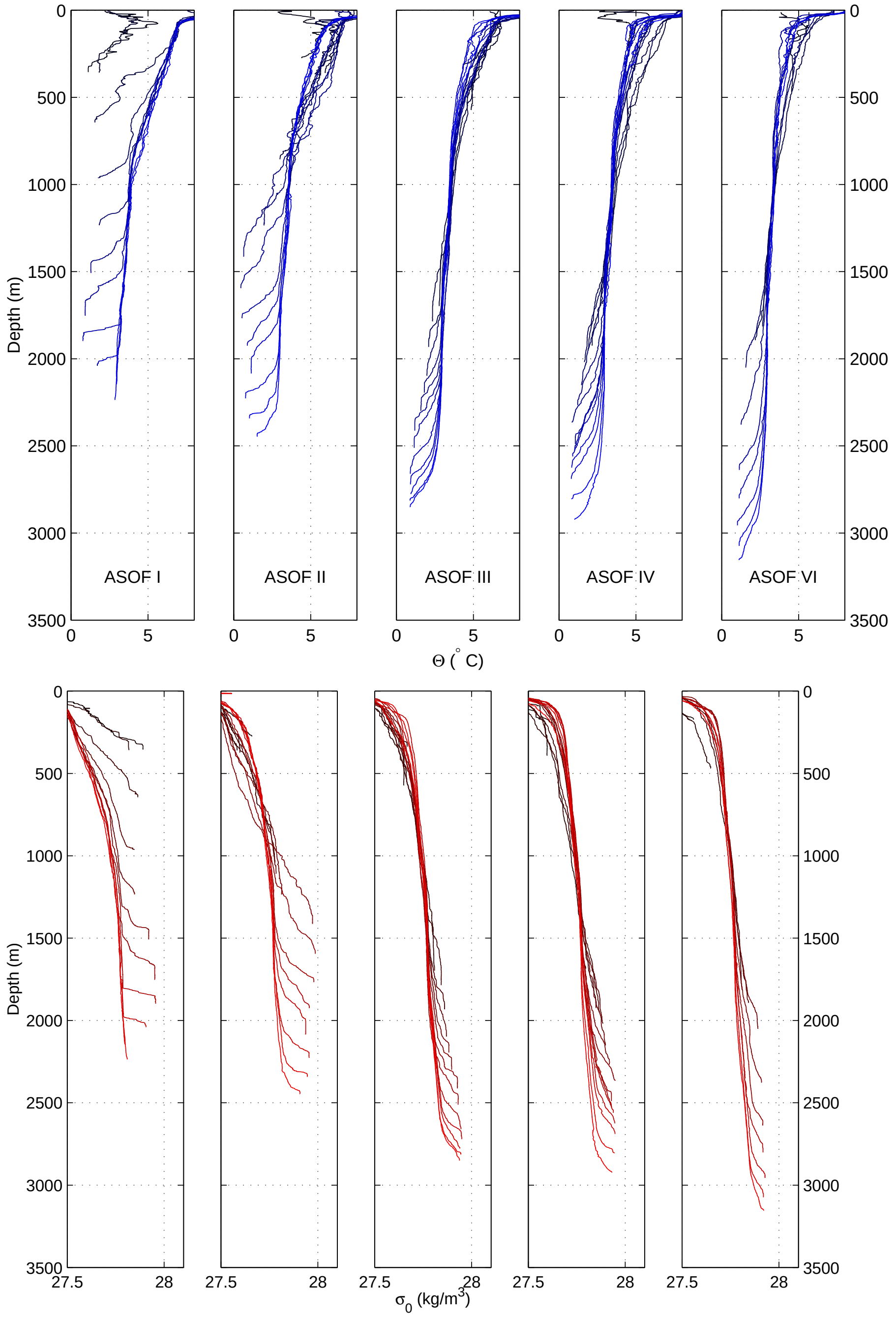

Figure 6.3: *Temperature profiles (upper panel) and density profiles (lower panel) for each ASOF standard section. Recorded on cruise M50/3 on* FS Meteor *from June 21. to July 15. 2001. The sharp interface between overflow plume and ambient water, apparent in both temperature and density profiles, is weakened on the way downstream.*

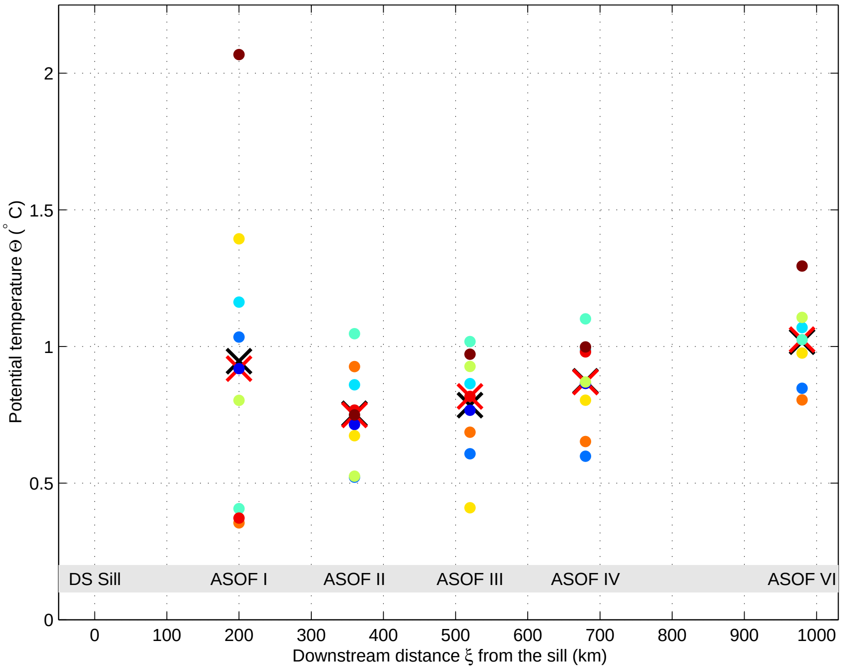

Figure 6.4: *Lowest bottom temperatures (round dots) from hydrographic sections 1997–2005. See text for calculation method. The colours give the year of the cruise, i. e. all values with the same colour belong to one hydrographic survey. Mean and median of each section are marked with black and red crosses, respectively.*

6.3 Downstream plume warming

The mean bottom temperatures derived from the temperature time series and hydrographic sections are both used to calculate a warming rate of the overflow plume with respect to the downstream distance. Fig. 6.5 shows a composite of the mean bottom temperatures that were calculated in the two preceding sections. The bottom temperatures from the mooring data are generally higher than those from the CTD sections. While the lowest bottom value is selected in each hydrographic section, the mooring time series are recorded at a fixed point and averaged over time.

The plume warming rate is calculated by a linear approximation of the mean temperatures. The slope of the linear fits gives the average plume warming rate. From the mooring values, the entrainment seems to be very strong on the first 200 km. Therefore the linear approximation is not applied to all the mooring values at once. It is distinguished between the way from the sill to the Dohrn array, where strong warming takes place, and the arrays thereafter. Hence, two warming rates are found. In the beginning, the strong entrainment leads to a warming rate of $442\,{}^{\mathrm{mK}}\!/_{100\,\mathrm{km}}$ while between the Dohrn and Angmagssalik arrays the warming rate is an order of magnitude smaller with $48\,{}^{\mathrm{mK}}\!/_{100\,\mathrm{km}}$. The warming rate is $112\,{}^{\mathrm{mK}}\!/_{100\,\mathrm{km}}$ when the vertical averaged mean temperatures between Dohrn and Angmagssalik are taken instead of the bottom values.

As discussed in the preceding section, the CTD values are problematic to use since the high variability leads to a decrease in temperature between sections ASOF I and ASOF II. The CTD values are approximated with and without the mean temperature from ASOF I, yielding plume warming rates of 17 and 44 $^{\mathrm{mK}}/_{100\,\mathrm{km}}$, respectively.

Instead of using the mean values from the CTD data, the lowest temperature from each section is chosen from the nine year long dataset to have another mean for the approximation of the plume warming rate. This method yields 54 $^{\mathrm{mK}}/_{100\,\mathrm{km}}$.

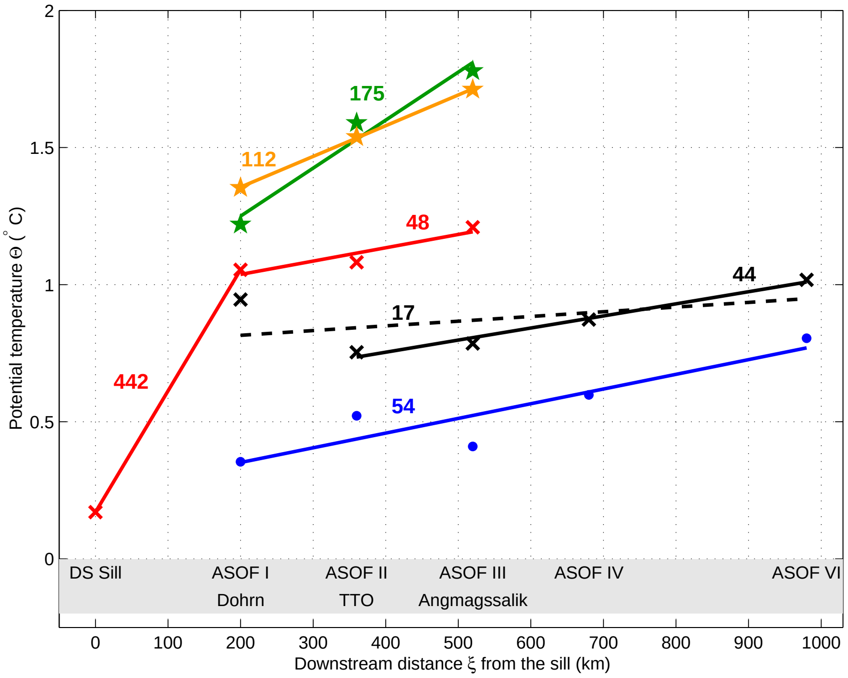

Figure 6.5: *Plume warming rates ($^{\mathrm{mK}}/_{100\,\mathrm{km}}$) from mean plume temperature. Mean bottom temperatures from mooring data (adopted from Fig. 6.1) are marked with red crosses. The mean temperatures given by* Saunders *(2001) are marked with green crosses. Vertical averaged mooring temperature values are plotted as orange stars. Mean bottom temperatures from CTD data (taken from Fig. 6.4) are marked with black crosses. The lowest value from each hydrographic section is shown with blue dots, additionally.*
The linear fit for the mooring bottom values is divided into two parts as there seem to be different entrainment regimes (red lines). The CTD values are linear fitted along all sections (dashed black line) and without section I (straight black line). The lowest values from the CTD data are approximated with a linear fit as well (blue line). The calculated plume warming rates, i. e. the slope of the fits, are printed to each line.

6.4 Summary and discussion

Data from moored thermometers and from hydrographic sections were used to calculate a pluming warming rate from mean plume temperatures. It could be found that

1. From the mooring time series, it appears that two entrainment regimes exist. On the first 200 km, the plume is warmed with a rate of $442\,\mathrm{mK}/100\,\mathrm{km}$, thereafter the warming rate decreases to $48\,\mathrm{mK}/100\,\mathrm{km}$. Vertical averaged mean plume temperatures yield a warming rate of $112\,\mathrm{mK}/100\,\mathrm{km}$ for this region.
2. The hydrographic data is strongly affected by the high variability of the overflow plume, especially close to the sill. The warming rates calculated from CTD sections range from 17 to $54\,\mathrm{mK}/100\,\mathrm{km}$, depending on the calculation method.

The calculation of the mean plume temperatures with bottom values yields a lower warming rate than the mean plume temperatures from vertical averaging. It can be concluded that the bottom layers of the plume are less mixed with ambient water than the upper layers.

7 Discussion

The meso-scale eddies in the Denmark Strait Overflow drive a heat transport that leads to a warming of the centre of the overflow plume. Using these heat transports and the mean downstream velocities of the plume, warming rates were estimated to $\sim 120\ {}^{\mathrm{mK}}/_{100\mathrm{km}}$ at the Dohrn array, $\sim 160\ {}^{\mathrm{mK}}/_{100\mathrm{km}}$ at the TTO array and $\sim 50\ {}^{\mathrm{mK}}/_{100\mathrm{km}}$ at the Angmagssalik array. This chapter relates the eddy induced warming rates to the overall plume warming seen in the hydrographic and the mooring temperature data. This gives an estimate for the contribution of meso-scale eddies to the entrainment into the overflow. Vertical mixing, the other component for driving the entrainment, is discussed. Finally, the results of this thesis are compared to entrainment rates found in previous studies.

The relative importance of eddy heat transports for the entrainment Plume warming rates along the downstream distance ξ were determined from

- horizontal heat fluxes driven by meso-scale eddies and
- mean plume temperatures from mooring timeseries and hydrographic sections.

In section 2.3.2, an averaged heat equation for temperature changes of the plume was derived:

$$c_p \bar{\rho} \bar{v} \frac{\partial \bar{T}}{\partial y} = c_p \bar{\rho} \cdot \left(\frac{\partial}{\partial x} \overline{u'T'} + \frac{\partial}{\partial z} \overline{w'T'} \right) + \epsilon$$

It states that the change in temperature along the path of the plume is to a large extent caused by horizontal and vertical turbulent heat fluxes. A comparison of the warming rates found here should therefore provide information about the relative importance of horizontal and vertical turbulent processes for the entrainment.

Fig. 7.1 compares the eddy driven warming rates for the three mooring arrays (first term on RHS) with the warming rates derived from mean plume temperatures (term on LHS) in chapter 6. The temperature increases strongly within the first 200 km from the sill. This could only be calculated from bottom mooring timeseries as no other data was available. Several estimates for the change of the mean temperature exist for the region further downstream. Here the warming rate from the near-bottom mooring timeseries is one order of magnitude less. It is very close to the warming rates from the hydrographic data that also estimate the change in near-bottom temperature. Vertical averaging of the mean temperature from mooring

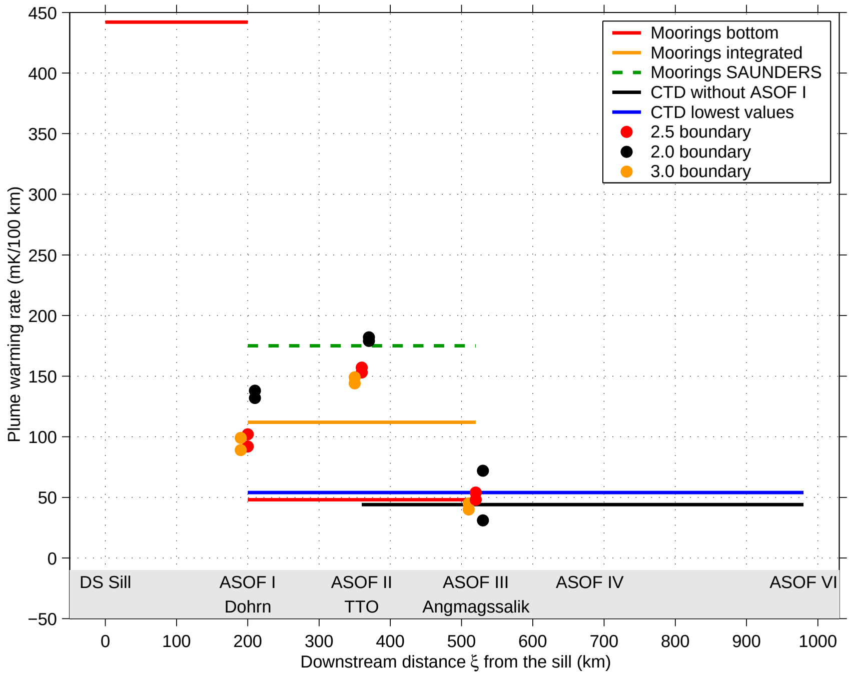

Figure 7.1: *Warming rates from mean plume temperatures (lines) and from eddy heat transports (dots). Eddy induced warming rates from the different plume boundary definitions (2.0, 2.5 and 3.0°C isotherm) are shown both for the polynomial and the linear interpolation method. The values from averaging over the part of the plume that has a convergence in eddy heat transport (see tables 4.2 and 5.1) are shown. The warming rate derived from the bottom values of the moorings (red lines) decreases at 200 km downstream distance.*

timeseries yields higher warming rates. However, they are still small compared to the warming rate closer to the sill.

The eddy induced warming rates shown in Fig. 7.1 (dots) are the mean values of the part of the plume that has a convergence in eddy heat transport. The eddy driven warming rates in the Dohrn and TTO arrays compare with the warming rates from the vertical averaged mean plume temperatures. In the Angmagssalik array, the eddy driven warming rates are smaller and compare with the rate of change of the near-bottom temperatures.

From the Dohrn to the Angmagssalik array, the eddy heat transports can explain most of the plume warming. The plume warming is associated with the entrainment in this study. Thus, the meso-scale eddies are the driving mechanism for the entrainment in the region further than 200 km from the sill. Unfortunately, no eddy warming rates between the sill and the Dohrn array could be calculated in this study. However, it is questionable whether eddies alone lead to a warming rate that is three to four times larger on the first 200 km behind the sill than in the mooring arrays analysed here. Thus, on the first 200 km behind the sill vertical processes should play an important role in the mixing.

The eddy induced warming rate is higher in the TTO than in the Dohrn array. This supports the finding of Käse et al. (2003) that between the Dohrn and the TTO array baroclinic instability enhances the eddy field. The decreasing vertical shear, manifested in a decrease of mean bottom speed from $50\,{}^{\mathrm{cm}}\!/\!_{\mathrm{s}}$ in the Dohrn array to $30\,{}^{\mathrm{cm}}\!/\!_{\mathrm{s}}$ in the TTO array, indicates the transfer of potential energy into eddy kinetic energy as described in section 2.2.2.

Vertical mixing A measure for the likelihood of vertical mixing is the dimensionless Richardson number. It is defined as

$$Ri = \frac{N^2}{\left(\frac{d\overline{u}}{dz}\right)^2} = \frac{\text{Potential energy}}{\text{Kinetic energy}} \tag{7.1}$$

where the Brunt-Väisälä frequency N is defined as

$$N^2 = -\frac{g}{\rho_0}\frac{d\overline{\rho}}{dz} \tag{7.2}$$

For discrete values, the Richardson number may be calculated as

$$Ri \approx \frac{(\rho_2 - \rho_1)\, gH}{\rho_0\,(U_1 - U_2)^2} \tag{7.3}$$

with U_i being the velocity of the layers, ρ_i the density of the water layers and H the height of the water column.

A stratified shear flow is stable if $Ri > {}^1\!/\!_4$. This criterion may not be met by the mean flow conditions, but there may still be events when $Ri < {}^1\!/\!_4$. The pulsation of the overflow plume could be such events.

An estimate from the current measurements and hydrographic sections gives a Richardson number in the Angmagssalik array that is considerably larger than one. Hence, there should be no or only few vertical instabilities leading to mixing. This is different closer to the sill. From CTD and XCP[1] sections between the sill and the Dohrn array (Girton, 2001), I estimate the Richardson number to be between 0.5 and 1. This is still above the $Ri > {}^1\!/\!_4$ criterion, but considering the high variability there may be times when the flow is vertically instable. Girton and Sanford (2003) find a similar pattern. Their mean Richardson number is 1.8 on the first 125 km downstream of the DS sill and only 1.2 thereafter. Here they find a large fraction of $Ri < 1$.

Entrainment regimes in the Denmark Strait Overflow From the results presented here, together with the findings from other studies, especially Girton (2001), Girton and Sanford (2003) and Käse et al. (2003), a picture of three different entrainment regimes in the Denmark Strait Overflow plume emerges.

---

[1] XCP: eXpendable Current Profiler, measures relative current velocities.

The *first regime* is located between the Denmark Strait sill and ∼125 km downstream of the sill. Here the plume accelerates from a mean speed of ∼20 cm/s at the sill to its maximum speed of∼60 cm/s. The current has a barotropic structure close to the sill, i. e. there is no strong shear between overflow plume and the watermasses above. Thus, little vertical turbulence should occur. The overall entrainment is estimated to be one order of magnitude smaller than beyond the 125 km mark. Meso-scale eddies are not visible at the surface yet. although, high variability in the bottom current with a dominant time-scale of 1.8 days (Smith, 1976) suggests that eddies are already generated in the overflow.

The region of strong entrainment into the overflow plume characterises the *second regime*. It reaches approximately to the Dohrn array 200 km downstream of the sill as indicated by the high plume warming rate (Fig. 6.5). The high plume velocities and the transition to a baroclinic flow lead to large vertical velocity shears. This shear and low Richardson numbers indicate vertical instability.

The transition to the *third regime* beyond 200 km downstream distance is characterised by the dominance of eddies in the entrainment process. The velocity shear provides the energy to feed baroclinic instabilities. The enhancement of the eddy field already starts at ∼125 km, but the eddy mixing becomes the dominant process for the entrainment into the overflow plume here. As the mean plume speed decreases, the velocity shear also decreases and the effect of vertical turbulence diminishes.

The picture of the three entrainment regimes is supported by the findings of Rudels et al. (1999). They observed a capping of the overflow plume with low salinity water that survived the initial descent of the plume. This suggests that vertical mixing is not taking place in the initial descent as the capping would be disturbed by the mixing. The low mixing matches with the first entrainment regime. As the plume reaches the second regime, the salinity minimum weakens.

Comparison with entrainment velocities in other studies The eddy heat transports into the overflow plume may be compared to the entrainment velocities calculated in Girton and Sanford (2003) and in Käse et al. (2003). The entrainment velocity is a fictitious quantity that describes the entrainment into the overflow plume. It does not distinguish between different processes. The calculation of a heat flux from the entrainment velocity w_e reads

$$\frac{\Delta Q}{\Delta t} = w_e \Delta T \rho c_p A. \tag{7.4}$$

Here ΔT is the temperature difference between plume and ambient water and A is the surface of the plume. For easy comparison with the eddy heat transports derived earlier, the surface A is chosen to have a length of 1 m. The boxes have a width of approximately 15 km, the surface A is $1.5 \cdot 10^4$ m^2.

Girton and Sanford (2003) found two entrainment velocities, $4{\cdot}10^{-5}$ m/s and $8{\cdot}10^{-4}$ m/s before and after 125 km downstream distance. Käse et al. (2003)

calculated an entrainment velocity of $5{\cdot}10^{-4}$ m/s in a numerical model. The heat transports per unit time for these entrainment velocities into a box with a width of 15 km are listed in table 7.1. The temperature difference ΔT is taken as 2 K.

The heat transports in entrainment regime I and III are of the same order of magnitude. The entrainment in the second regime is one order of magnitude higher. The warming rates in table 7.1 support the hypothesis of the three entrainment regimes.

Table 7.1: *Heat transport per unit time $\Delta Q/\Delta t$ (J/s) into a box of 15 km width, calculated from the entrainment velocities in* GIRTON AND SANFORD *(2003) and* KÄSE ET AL. *(2003). The temperature difference between overflow plume and ambient water is taken as 2 K. The entrainment regimes proposed earlier are given for all values.*

Entrainment regime	Entrainment velocity	Heat transport
GIRTON AND SANFORD (2003)		
I	$4{\cdot}10^{-5}$ m/s	48 J/s
II	$8{\cdot}10^{-4}$ m/s	960 J/s
KÄSE ET AL. (2003)		
I and II	$5{\cdot}10^{-4}$ m/s	900 J/s
This study		
III		10 J/s to 100 J/s

8 Perspectives

The Atlantic Meridional Overturning Circulation and its associated heat transport from low to high latitudes strongly influences the climate over Northern Europe. Its possible weakening in the course of climate change calls for a better understanding of the driving and modifying processes.

The convective regions in the Northern Seas and the Labrador Sea and the dense overflows across the Greenland-Scotland Ridge have been subject to numerous studies. Their fundamental processes are understood and have been reproduced in numerical models. While the contribution of entrainment to the overall transport of watermasses in the overturning circulation has been estimated to about $^1/_3$ of the total amount, the processes that lead to the observed entrainment are not very well understood yet.

In the work described in this thesis it was found that warming induced by meso-scale eddies provides the dominant contribution to the entrainment into the Denmark Strait overflow plume 200 km downstream of the sill and beyond (entrainment regime III). General circulation models used in climate prediction studies are often too coarse to resolve processes with these scales. The results presented here suggest that numerical simulations of the overturning circulation should include meso-scale processes in the overflows. This calls for a better resolution of the overflow regions in large scale simulations.

The understanding of the entrainment process is also needed to estimate the impact of changing conditions in the sinking regions, where the dense waters feeding the overflows are produced. A reduced dense water reservoir in the Nordic Seas will lead to a reduction of the transports across the Greenland-Scotland Ridge. Whether this trend is intensified or balanced by a change in the eddy fields is a fascinating issue that calls for an even better observation and understanding of the entrainment processes. Plans and suggestions for such observations are listed below.

- The entrainment of ambient water into the overflow plume is strong in the first 200 km downstream of the Denmark Strait sill. Moorings in the second entrainment regime would improve the understanding of the eddy generation process and provide information on the role of the eddies in this region.
- The role of vertical warming is estimated here as the residual of the plume warming that is not covered by the eddy driven heat transports. This estimate can certainly be improved. Measurements in the Denmark Strait Overflow with a microstructure instrument are planned for a cruise with *RRS Discovery*

in autumn 2006. The instrument measures dissipation-scale turbulence. The vertical eddy diffusivities can be determined from the measured microstructure velocity shear.

- The mean eddy heat fluxes in the mooring arrays have a pronounced vertical structure. At most of the moorings the direction of the mean eddy heat flux changes with height above bottom. This is not properly resolved with the three or four instruments at each mooring line. Measurements with an ADCP[1] would give the vertical velocity structure with a higher resolution.
- The barotropic structure of the eddies leads to a high variability of the sea surface height (SSH) which can be observed by altimetry satellites. HØYER AND QUADFASEL (2001) showed that the fluctuating SSH gives a signature of the overflow regions in Denmark Strait and the Faroe Bank Channel at the sea surface. Altimetry measurements may thus be used to monitor the the entrainment process in the deep if a correlation between SSH and eddy induced entrainment existed.

---

[1] Acoustic Doppler Current Profiler

A Abbreviations

ADCP	Acoustic Doppler Current Profiler
AIW	Arctic Intermediate Water
AMOC	Atlantic Meridional Overturning Circulation
BBL	Bottom Boundary Layer
CEFAS	The Centre for Environment, Fisheries and Aquaculture Science
CTD	Conductivity-Temperature-Depth sensor
DS	Denmark Strait
DSO	Denmark Strait Overflow
DSOW	Denmark Strait Overflow Water
EGC	East Greenland Current
FBC	Faroe Bank Channel
GSR	Greenland-Scotland Ridge
ISOW	Iceland-Scotland Overflow Water
ISW	Irminger Sea Water
MOC	Meridional Overturning Circulation
NAC	North Atlantic Current
NADW	North Atlantic Deep Water
PSD	Power Spectral Density
PV	Potential Vorticity
TTO	Transient Tracers in the Ocean

Bibliography

AAGAARD, K. and S.-A. MALMBERG. Low-frequency Characteristics of the Denmark Strait Overflow. *ICES CM*, 1978.

ASOF-W. Final Scientific Report. 2006.

BIASTOCH, A., R. H. KÄSE and D. B. STAMMER. The Sensitivity of the Greenland-Scotland Ridge Overflow to Forcing Changes. *Journal of Physical Oceanography*, **33**, 2307–2319, 2003.

BRUCE, J. G. Eddies southwest of the Denmark Strait. *Deep-Sea Research I*, **42**, 13–29, 1995.

BRYDEN, H. L., H. R. HANNAH R. LONGWORTH and S. A. CUNNINGHAM. Slowing of the Atlantic meridional overturning circulation at 25° N. *Nature*, **438**, 655–657, 2005.

CENEDESE, C., J. A. WHITEHEAD, T. A. ASCARELLI and M. OHIWA. A Dense Current Flowing down a Sloping Bottom in a Rotating Fluid. *Journal of Physical Oceanography*, **34**, 188–203, 2003.

CUSHMAN-ROISIN, B. *Introduction to Geophysical Fluid Dynamics*. Prentice-Hall, 1994.

DICKSON, R. R. and J. BROWN. The production of North Atlantic Deep Water: Sources, rates, and pathways. *Journal of Geophysical Research*, **99**, 12319–12341, 1994.

EMERY, W. J. and R. E. THOMSON. *Data Analysis Methods in Physical Oceanography*. Elsevier, 1998.

ETLING, D., F. GELHARDT, U. SCHRADER, F. BRENNECKE, G. KÜHN, G. C. D'HIERES and H. DIDELLE. Experiments with density currents on a sloping bottom in a rotating fluid. *Dynamics of Atmospheres and Oceans*, **31**, 139–164, 2000.

GIRTON, J. B. *Dynamics of transport and variability in the Denmark Strait overflow*. Ph.D. thesis, University of Washington, Seattle, WA, 2001.

GIRTON, J. B. and T. B. SANFORD. Descent and Modification of the Overflow Plume in the Denmark Strait. *Journal of Physical Oceanography*, **33**, 1351–1364, 2003.

HANSEN, B. and S. ØSTERHUS. North Atlantic - Nordic Sea exchanges. *Progress in Oceanography*, **45**, 109–208, 2000.

HANSEN, B., S. ØSTERHUS, D. QUADFASEL and W. TURRELL. Already the Day After Tomorrow? *Science*, **305**, 953–954, 2004.

HANSEN, B., W. R. TURRELL and S. ØSTERHUS. Decreasing overflow from the Nordic seas into the Atlantic Ocean through the Faroe Bank channel since 1950. *Nature*, **416**, 927–930, 2001.

HØYER, J. L. and D. QUADFASEL. Detection of deep overflows with satellite altimetry. *Geophysical Research Letters*, **28**, 1611–1614, 2001.

JIANG, L. and R. W. GARWOOD. Three-Dimensional Simulations of Overflows on Continental Slopes. *Journal of Physical Oceanography*, **26**, 1214–1233, 1996.

JÓNSSON, S. and H. VALDIMARSSON. A new path for the Denmark Strait overflow water from the Iceland Sea to Denmark Strait. *Geophysical Research Letters*, **31**, L03305, 2004.

JUNGCLAUS, J. H., J. HAUSER and R. H. KÄSE. Cyclogenesis in the Denmark Strait Overflow Plume. *Journal of Physical Oceanography*, **31**, 3214–3229, 2001.

KÄSE, R. H., J. B. GIRTON and T. B. SANFORD. Structure and variability of the Denmark Strait Overflow: Model and observations. *Journal of Geophysical Research*, **108**, 12–1–12–15, 2003.

KÄSE, R. H. and A. OSCHLIES. Flow through Denmark Strait. *Journal of Geophysical Research*, **105**, 28527–28546, 2000.

KNAUSS, J. A. *Introduction to Physical Oceanography*. Prentice-Hall, 2nd edition, 1997.

KÖHL, A., R. KÄSE, D. STAMMER and N. SERRA. Causes of changes in the Denmark Strait Overflow. *Journal of Physical Oceanography (submitted)*, 2006.

KRAUSS, W. *Methods and Results of Theoretical Oceanography, Vol. I - Dynamics of the Homogeneous and the Quasihomogeneous Ocean*. Gebrüder Borntraeger, Berlin, 1973.

KRAUSS, W. A note on overflow eddies. *Deep-Sea Research I*, **43**, 1661–1667, 1996.

KRAUSS, W. and R. H. KÄSE. Eddy formation in the Denmark Strait overflow. *Journal of Geophysical Research*, **103**, 15525–15538, 1998.

Kundu, P. K. *Fluid Mechanics*. Academic Press, 1990.

Lane-Serff, G. F. and P. G. Baines. Eddy Formation by Overflows in Stratified Water. *Journal of Physical Oceanography*, **30**, 327–337, 2000.

Macrander, A. *Variability and Processes of the Denmark Strait Overflow*. Ph.D. thesis, Christian-Albrechts-Universität Kiel, 2004.

Macrander, A., U. Send, H. Valdimarsson, S. Jónsson and R. H. Käse. Interannual changes in the overflow core from the Nordic Seas into the Atlantic Ocean through Denmark Strait. *Geophysical Research Letters*, **32**, L06606, 2005.

Pawlowicz, R., B. Beardsley and S. Lentz. Classical tidal harmonic analysis including error estimates in MATLAB using T_TIDE. *Computers & Geosciences*, **28**, 929–937, 2002.

Price, J. F. and M. O. Baringer. Outflows and deep water production by marginal seas. *Progress in Oceanography*, **33**, 161–200, 1994.

Rudels, B., P. Eriksson, H. Grönvall, R. Hietala and J. Launiainen. Hydrographic Observations in Denmark Strait in Fall 1997, and their Implications for the Entrainment into the Overflow Plume. *Geophysical Research Letters*, **26**, 1325–1328, 1999.

Rudels, B., E. Fahrbach, J. Meincke, G. Budéus and P. Eriksson. The East Greenland Current and its contribution to the Denmark Strait overflow. *ICES Journal of Marine Science*, **59**, 1133–1154, 2002.

Saunders, P. M. The Dense Northern Overflows. In Siedler, Church and Gould, editors, *Ocean Circulation & Climate*, volume 77, pages 401–417. International Geophysics Series, 2001.

Smith, P. C. A streamtube model for bottom boundary currents in the ocean. *Deep-Sea Research*, **22**, 853–873, 1975.

Smith, P. C. Baroclinic Instability in the Denmark Strait Overflow. *Journal of Physical Oceanography*, **6**, 355–371, 1976.

Smith, W. H. F. and D. T. Sandwell. Global sea floor topography from satellite altimetry and ship depth soundings. *Science*, **277**, 1956–1962, 1997.

Spall, M. A. and J. F. Price. Mesoscale Variability in Denmark Strait: The PV Outflow Hypothesis. *Journal of Physical Oceanography*, **28**, 1598–1623, 1998.

Swift, J. H., K. Aagaard and S. Malmberg. The contribution of the Denmark Strait overflow to the deep North Atlantic. *Deep-Sea Research*, **27A**, 29–42, 1980.

Tanhua, T., K. Bulsiewicz and M. Rhein. Spreading of overflow water from the Greenland to the Labrador Sea. *Geophysical Research Letters*, **32**, L10605, 2005.

Whitehead, J. A. Topographic control of oceanic flows in deep passages and straits. *Reviews of Geophysics*, **36**, 423–440, 1998.

Whitehead, J. A., M. E. Stern, G. R. Flierl and B. A. Klinger. Experimental Observations of Baroclinic Eddies on a Sloping Bottom. *Journal of Geophysical Research*, **95**, 9585–9610, 1990.

Worthington, L. V. An attempt to measure the volume transport of Norwegian Sea overflow water through the Denmark Strait. *Deep Sea Research, 1969*, **16, supplement**, 421–432, 1969.

Acknowledgements

First and foremost I want to thank my supervisor Detlef Quadfasel for his outstanding support with this thesis. His ideas and comments were a great help. He had time whenever I had a question and did a great job in introducing me to oceanographic research.

Thanks to Prof. Robert L. Johnson for reviewing this thesis.

Thanks to John Mortensen for help with scientific questions as well as an excellent cruise with whales, icebergs and rotten shark.

Stephen Dye was a perfect workmate in the shifts on the *Arni Fridriksson.* He provided me with the most recent mooring data.

Ulrich Drübbisch introduced me into the mooring work during the cruise.

Thanks to all the people that worked on collecting the data used in this thesis.

I want to whish Maddis, Martin, Ole and Philipp all the best with their theses.

Many thanks to my parents for support in many ways.

And thank you Olga for being with me.

Erklärung

Hiermit erkläre ich, dass ich meine Diplomarbeit selbständig und nur unter Verwendung der angegebenen Quellen und Hilfsmittel verfasst habe.

Mit einer Aufnahme der Arbeit in die Bibliothek bin ich einverstanden.

Hamburg, den 31. August 2006

(Gunnar Voet)